РОССИЙСКИЙ ГОСУДАРСТВЕННЫЙ ПЕДАГОГИЧЕСКИЙ УНИВЕРСИТЕТ им. А. И. ГЕРЦЕНА
HERZEN STATE PEDAGOGICAL UNIVERSITY of RUSSIA

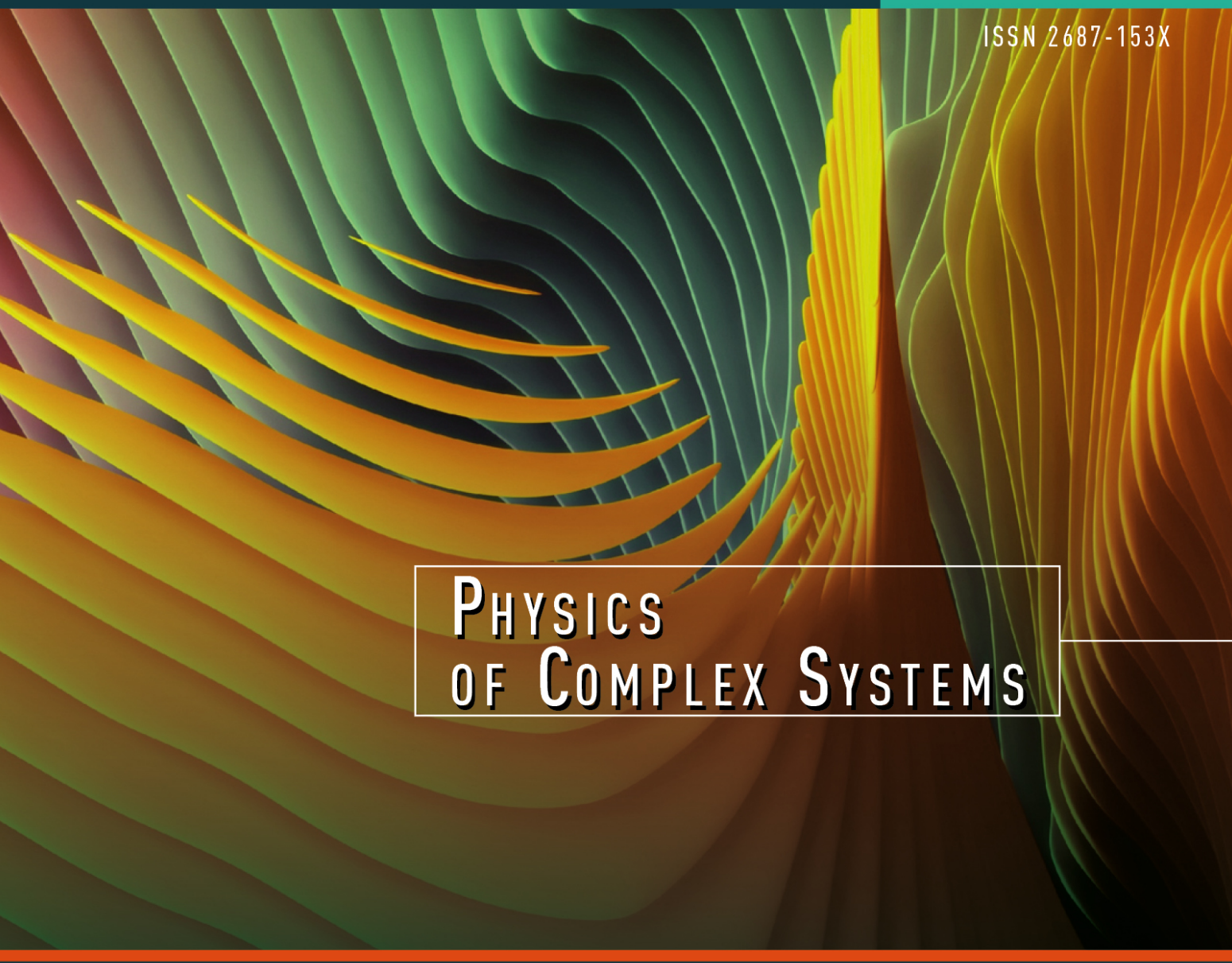

ISSN 2687-153X

Physics of Complex Systems

Т. 1 № 4 2020

Vol. 1 No. 4 2020

Herzen State Pedagogical University of Russia

physcomsys.ru
ISSN 2687-153X (online)
DOI 10.33910/2687-153X-2020-1-4
2020. Vol. 1, no. 4

PHYSICS OF COMPLEX SYSTEMS

Mass Media Registration Certificate El No. FS77-77889, issued by Roskomnadzor on 10 February 2020
Peer-reviewed journal
Open Access
Published since 2020
4 issues per year

Publishing house of Herzen State Pedagogical University of Russia
48 Moyka Emb., St Petersburg 191186, Russia
E-mail: izdat@herzen.spb.ru
Phone: +7 (812) 312-17-41

Data size 5,20 Mbyte
Published at 22.12.2020

Editors of the English text *I. A. Nagovitsyna, M. V. Bumakova*
Cover design by *O. V. Rudneva*
Layout by *A. M. Khodan, L. N. Kliuchanskaya*

Saint Petersburg, 2020

CONTENTS

Condensed Matter Physics **129**

Kolesnikova A. L., Rozhkov M. A., Abramenko N. D., Romanov A. E. On mesoscopic description of interfaces in graphene 129

Nikonorova N. A., Kononov A. A., Castro Arata R. A. Molecular mobility in crystallising aromatic thermoplastic polyimide R-BAPS 135

Gasumyants E. V. The calcium effect on the thermopower, critical temperature and charge-carrier system parameters in the $Y_{0.75-x}Ca_xPr_{0.25}Ba_2Cu_3O_y$ HTSC-syrtem 142

Theoretical Physics **150**

Liaptsev A. V. Linear properties of chaotic states of systems described by equations of nonlinear dynamics: Analogy with quantum theory 150

Vorobiev A. M., Yurova T. S., Popov I. Y. A model of a quantum waveguide multiplexer 158

Potkina M. N., Lobanov I. S., Uzdin V. M. Fine energy structure of a magnetic skyrmion localized on a nonmagnetic impurity in an external magnetic field 165

Condensed Matter Physics.
Physics of Low-Dimensional Structures and Nanostructures

UDC 547.022.1/.4 DOI: 10.33910/2687-153X-2020-1-4-129-134

On mesoscopic description of interfaces in graphene

A. L. Kolesnikova[1], M. A. Rozhkov[2], N. D. Abramenko[2], A. E. Romanov[✉2]

[1] Institute for Problems in Mechanical Engineering of the Russian Academy of Sciences, 61 Bolshoy Ave., Vasilievsky Island, Saint Petersburg 199178, Russia
[2] ITMO University, 49 Kronverksky Ave., Saint Petersburg 197101, Russia

Authors

Anna L. Kolesnikova, ORCID: 0000-0003-4116-4821, e-mail: anna.kolesnikova.physics@gmail.com

Mikhail A. Rozhkov, ORCID: 0000-0001-7350-0717

Nikita D. Abramenko

Alexey E. Romanov, ORCID: 0000-0003-3738-408X

For citation: Kolesnikova, A. L., Rozhkov, M. A., Abramenko, N. D., Romanov, A. E. (2020) On mesoscopic description of interfaces in graphene. *Physics of Complex Systems*, 1 (4), 129–134. DOI: 10.33910/2687-153X-2020-1-4-129-134

Received 13 October 2020; reviewed 6 November 2020; accepted 7 November 2020.

Funding: The work was supported by the Russian Foundation for Basic Research (grant No. 18-01-00884 A).

Abstract. The article discusses a mesoscopic approach to the description of interfaces (IFs) in graphene. The approach is based on the representation of defective carbon rings with broken six-fold symmetry in hexagonal lattice of graphene as singular defects, i.e. wedge disclinations, in an elastic continuum. The angle of the sector inserted into or removed from the hexagonal lattice that results in the formation of localized quadrate, pentagon, heptagon, and octagon carbon rings, defines the strength (charge) of disclinations. The mesoscopic approach views IF in graphene as an ensemble of disclinations distributed along a line. Elementary building blocks for IFs with periodic motives of carbon atoms are structural units (SUs) containing disclination sets with zero total disclination charge. The junction of SUs of different type is considered as a virtual disclination. The approach works well in graphene when analyzing elastic fields and stored energies of IFs of two types: grain boundaries (GBs) that induce misorientation of neighboring domains of graphene lattice, and zero misorientation interfaces (ZMIs) that do not possess such a property.

Keywords: graphene, crystal lattice defects, elastic continuum, disclinations, interfaces, structural units.

Introduction

One of the most important scientific discoveries of the early 21st century is the successful production of graphene, a two-dimensional carbon crystal with a hexagonal lattice (Geim, Novoselov 2010). This fact, as well as the unique properties of graphene, gave rise to works on the synthesis, analysis and modelling of new two-dimensional materials with desired properties, see, for example, recent publications in Nature Communications (Tang et al. 2019) and Scientific Reports (Bravo et al. 2019; Wang et al. 2019). Graphene has high strength and plasticity (Frank et al. 2007; Lee et al. 2008), special electronic properties due to the presence of a Dirac cone in its band structure (Avouris 2010; Castro Neto et al. 2009), and a record high thermal conductivity (Balandin et al. 2008). These characteristics allow to consider graphene as a material for next-generation electronics and optoelectronics.

Physical and mechanical properties of graphene are significantly affected by defects in its crystal lattice, in particular, linear defects—interfaces (IFs), see Ref. (Bagri et al. 2011; Ovid'ko 2013; Romanov et al. 2018). At present, there are well-developed atomistic methods for studying defects in graphene: molecular dynamics (MD) simulation technique operating with empirical interatomic potentials, and

the density functional theory (DFT) approach based on first principle calculations for atomic systems. The other methods known as mesoscopic ones consider defects in a continuum with prescribed effective properties of graphene.

In our previous studies of defects in graphene we used both atomistic modelling methods and tools of the continuum theory of solids (Kolesnikova et al. 2017; 2020; Romanov et al. 2018; Rozhkov et al. 2016; Rozhkov, Kolesnikova, Hussainova et al 2018; Rozhkov, Kolesnikova, Yasnikov et al. 2018). In this work, based on the theory of disclinations in an isotropic elastic continuum, we use a mesoscopic approach to analyze graphene IFs.

Disclinations in graphene

In the framework of mesoscopic approach, a single carbon pentagon (five-member carbon ring) in otherwise hexagonal graphene lattice points to the core of a positive 60-degree wedge disclination. Indeed, the removal of the 60-degree wedge from the graphene lattice consisting of six-member carbon rings leads to the appearance of a wedge disclination with a strength of $\omega = 60^\circ = +\pi/3$. The atoms nearest to the disclination point form a pentagon, and the entire graphene lattice is elastically distorted (Fig. 1). In a similar manner, one can imagine carbon quadrate (Fig. 1). Unlike the pentagon, the heptagon serves as the core of a negative 60-degree disclination, as its appearance is a consequence of the insertion of the 60-degree wedge into the hexagonal graphene lattice (Fig. 1). Embedding of $60n$ -degree wedge (n = 2, 3, ...) into graphene lattice leads to the negative wedge disclination of the corresponding strength with a core in the form of an octagon, a nonagon, etc. (Fig. 1) (Kolesnikova et al. 2017; Romanov et al. 2018; Rozhkov et al. 2016; Rozhkov, Kolesnikova, Yasnikov et al. 2018; Harris 1977).

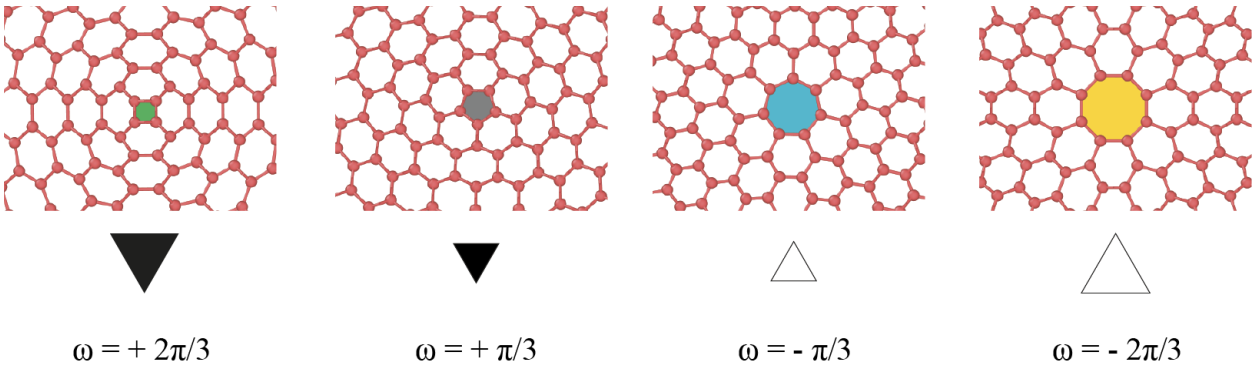

Fig. 1. Defective carbon polygons in graphene lattice and their relation to disclinations.
The strength ω of positive and negative disclinations is denoted below the corresponding schematics

Single isolated wedge disclinations cause enormous elastic distortions that scale logarithmically with the distance from their cores and have their energies proportional to R^2, where R is the crystallite size (Romanov, Vladimirov 1992). In case of graphene sheets, the elastic energy diminishes when disclination approaches to the edge of the sheet that is similar to the screening of disclination elastic fields by a free surface in case of 3D-crystals (Romanov, Vladimirov 1992). Changing the geometry of the graphene sheet, i.e. the formation of a curved carbon shell, provides the release of disclination elastic energy. In the extreme case, closed spherical-alike carbon shell with twelve positive wedge disclinations of strength $\omega = +\pi/3$ each form fullerene macromolecule (Kolesnikova, Romanov 1998).

In the flat graphene sheet, disclinations of opposite sign can form self-screened configurations, whose energies do not depend on the crystallite size. Such configurations have zero disclination charge and zero dipole moment (Romanov, Vladimirov 1992):

$$\sum_i \omega_i = 0, \tag{1a}$$

$$\sum_i \omega_i \boldsymbol{r}_i = 0, \tag{1b}$$

where ω_i is the strength of the i-th disclination in the ensemble, $\boldsymbol{r}_i$ is the radius-vector from the coordinate origin to the i-th disclination.

 DOI: 10.33910/2687-153X-2020-1-4-129-134

Important examples of screened disclination configurations are disclination quadrupoles and their ensembles, for which the conditions (1a, b) are fulfilled, see, e.g. Ref. (Rozhkov, Kolesnikova, Yasnikov et al. 2018). Interfaces in graphene consisting of periodic chains of disclinated carbon polygons (Ovid'ko 2013; Romanov et al. 2018) give other examples of screened disclination ensembles satisfying Eqs. (1a, b).

Interfaces in graphene

In our earlier work, see Ref. (Romanov et al. 2015), it was established that the grain boundaries (GBs) in graphene consist of structural units (SUs), which are well-defined motives (or combinations) of disclinated and regular carbon rings. Then the concept of SUs was extended to all periodic straight-linear IFs in graphene (Kolesnikova et al. 2017; Romanov et al. 2018; Rozhkov et al. 2016).

Structural units of periodic interfaces in graphene

Figure 2 shows selected SUs from a wide range of possible SUs and their disclination schematics. The nomenclature for a SU includes numbers that denote the types of disclinated carbon rings, e.g. 4—quadrat, 5—pentagon, 7—heptagon etc., and letters (sometimes with a number) denoting a modification for combining these carbon rings into a SU.

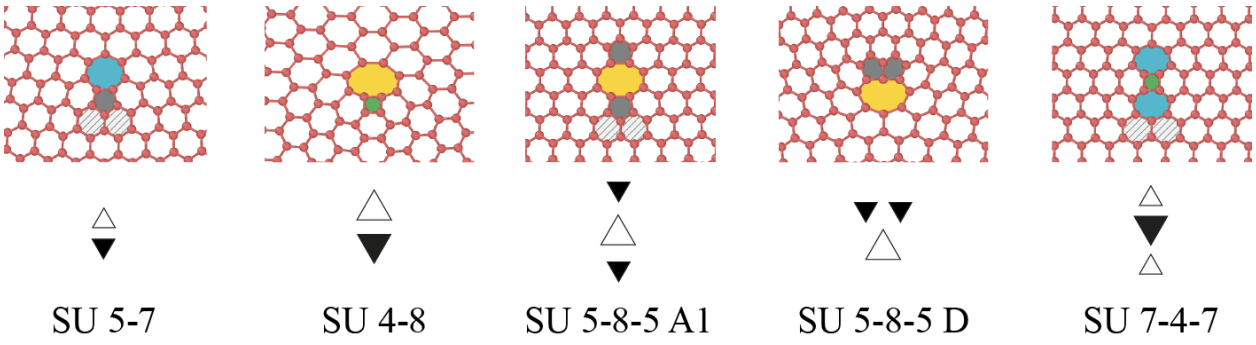

Fig. 2. Typical structural units (SUs) of interfaces in graphene and their disclination schematics. The filled carbon rings belong to the shown SUs

Structural units that may construct interfaces in graphene meet two major requirements:

(a) SUs have to form the interface without breaking the bonds and without changing the type of the bond (sp^2 hybridization for graphene) when joining. Some SUs contain additional hexagonal carbon rings typical for the defect-free graphene crystal lattice, see SU 5—7, SU 5—8—5 A1, SU 7—4—7 with the shaded hexagons in Fig. 2. This allows to construct straight-linear interfaces.

(b) SUs have to obey the rule of Eq. (1a), i.e. they must have zero disclination charge.

We note that the condition (1b) is not required for a single SU. This condition has to be satisfied when connecting SUs into the linear periodic chain—the interface. For example, SU 5—8—5 A1 and SU 7—4—7, according to their disclination schematics, are the disclination quadrupoles and, therefore, have both properties (1a, b) (Romanov, Vladimirov 1992; Rozhkov, Kolesnikova, Yasnikov et al. 2018), while SU 5-7, SU 4—8 and SU 5—8—5 D have property (1a), only.

Disclination schematics for interfaces in graphene

Figure 3 shows typical straight-linear IFs in graphene. These interfaces are composed of closely packed SUs shown in Fig. 2, they are marked correspondingly. Interface 5—7 is the so-called "favorite" grain boundary (GB) with misorientation angle $\theta = 21.8^\circ$, see, e.g. Refs. (Romanov et al. 2015; Zhang, Zhao 2013). All other IFs in Fig. 3 are zero misorientation IFs.

For each atomistic IF configuration, its disclination scheme is given. The splitting of IF disclination content into disclination quadrupoles is highlighted with dashed ellipses in the same Fig. 3. As a result of such subdivision, IF structure can be modelled with a set of periodically distributed disclination quadrupoles. Therefore, we conclude that in addition to the property defined by Eq. (1a) straight-linear IFs in graphene possess the property given by Eq. (1b). Note that SUs are not necessarily equivalent to the defined disclination quadrupoles in IFs, they are just building blocks for an IF atomistic structure whereas quadrupoles relate to the mesoscopic description of IFs.

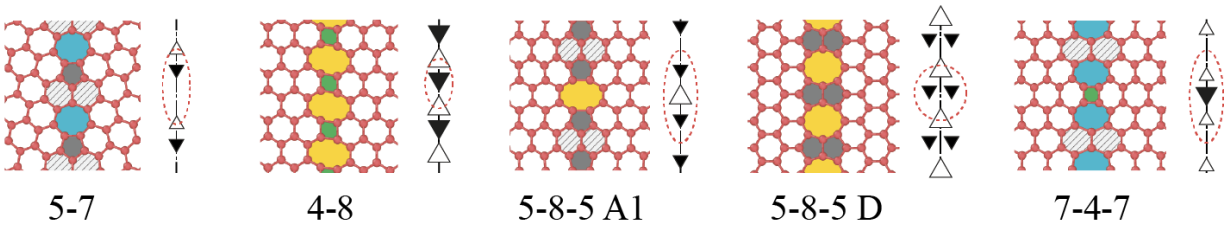

Fig. 3. Straight-linear interfaces in graphene and their disclination content. In disclination schematics, quadrupole configurations are highlighted with dashed-line ellipses

Elastic fields and elastic energy of interfaces in graphene

Figure 3a gives mesoscopic disclination description of IFs. It allows to calculate their elastic fields: displacements, strains and stresses using analytical relationships of disclination theory (Kolesnikova et al. 2014; Romanov, Vladimirov 1992). For such calculations graphene elastic constants, i. e. Poisson's ratio ν and shear modulus G have to be determined in experiments or be extracted from the atomistic simulations.

Defining disclination quadrupole content of IFs we estimate their elastic energies with the help of analytical formulas for quadrupole energies (Romanov, Vladimirov 1992). Starting with the energy of a single quadrupole one gets a rough approximate value for the energy per unit length of the interface, which can be then refined by accounting for the interactions of neighboring quadrupoles, next to the neighboring ones, etc. For example, IF 5—8—5 D energy per unit length will be $E_{5-8-5D} = 1.032$ eV/Å when accounting for the energy of a single quadrupole, and $E_{5-8-5D} = 0.757$ eV/Å when considering pair interactions among disclinations quadrupoles. In this mesoscopic analysis we used Poisson ratio ν and shear modulus G found by the MD simulation with AIREBO potential of defect-free graphene: ν = 0.367 and G = 367 GPa, respectively. Atomistic MD modelling for the same interface gives the value $E_{5-8-5D} = 0.626$ eV/Å. The above example demonstrates that the mesoscopic approach works quite well for the analysis of elastic properties of IFs in graphene.

Grain boundaries in graphene as the walls of virtual disclination dipoles

According to the approach developed for metals (Gertsman et al. 1989; Nazarov et al. 1993) and applied to graphene (Romanov et al. 2015), each favored grain boundary (GB) consists of only one type of SUs; each arbitrary GB with a misorientation angle θ consists of only two types of SUs belonging to the two nearest favored GBs, denoted as "r" and "r + 1", with misorientations θ_r and θ_{r+1} (r = 1, 2…). Since the junctions of SUs with different misorientations by definition form disclinations, the structure of arbitrary GB is described as a wall of *virtual* disclination dipoles, in which the arm of the dipoles depends on θ , and it is equal or multiples to d_A or d_B , where d_A and d_B are the lengths of SUs A and B corresponding to GB_r and GB_{r+1}, respectively (Gertsman et al. 1989).

In the mesoscopic disclination-structural unit model of the structure of arbitrary GB, disclination dipoles will be distributed periodically with the shortest period $H = md_A + nd_B$, where m and n are the numbers of SUs forming the period, or the larger period $H_k = kH$, where k is an integer. Inside the period the distribution of the disclination dipoles is nonuniform. The average misorientation angle can be determined with good accuracy from a simple expression:

$$\theta \cong \frac{md_A\theta_r + nd_B\theta_{r+1}}{H}. \quad (3)$$

In the framework of the disclination-structural unit model, the total energy E per unit length of the GB in 2D crystal is calculated as the sum of three terms (Nazarov et al. 1993):

$$E = E_0 + E_{elastic} + E_{core}, \quad (4)$$

where E_0 is the GB average interface energy, $E_{elastic}$ is the elastic energy of the disclination ensemble, and E_{core} is the energy of disclination cores. All energies are considered as the energies per unit length of GB.

 DOI: 10.33910/2687-153X-2020-1-4-129-134

Shown in left column in Fig. 3 and in Fig. 4 GB 5–7 is composed of SU 5–7 only, hence the description "favorite". Using SU 5–7 of the two modifications *B* (*B*'), and structural units of the degenerate type, consisting of hexagons only, *A* and *C*, any geometrical configuration for arbitrary GB can be constructed, see examples of GBs with $\theta = 13.2^\circ$ and $\theta = 26.1^\circ$ in Fig. 4. Following this procedure we find the distribution of SUs and the disclination dipoles for GBs in graphene with the misorientation in the range $0–60^\circ$, which is divided by the favored GB into two intervals $0^\circ < \theta < 21.8^\circ$ and $21.8^\circ < \theta < 60^\circ$, see Fig. 4.

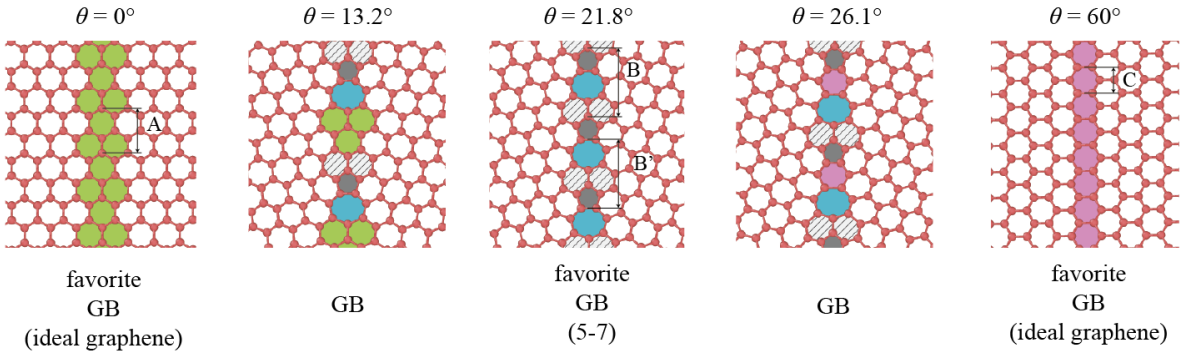

Fig. 4. Symmetrical tilt GBs in graphene, composed with structural units A, B (B'), and C. Favored GBs made of SUs of a single type with misorientation angles $\theta = 0°$, 21.8°, and 60°; arbitrary GBs made of SUs of two types with misorientation angles $\theta = 13.2°$ and 26.1°

Misorientation angle for any arbitrary GB is calculated using Eq. (3):

$$\theta \cong \frac{md_A\theta_A + nd_B\theta_B}{md_A + nd_B}, \quad 0^\circ < \theta < 21.8^\circ, \tag{5a}$$

$$\theta \cong \frac{md_B\theta_B + nd_C\theta_C}{md_B + nd_C}, \quad 21.8^\circ < \theta < 60^\circ, \tag{5b}$$

where m and n are the numbers of the structural units in the period $H = md_A + nd_B$ (or $H = md_B + nd_C$) of GB, $\theta_A = 0^\circ$, $\theta_B = 21.8^\circ$, and $\theta_C = 60^\circ$; $d_A \approx 3a$, $d_B \approx \sqrt{21}a$, and $d_c \approx \sqrt{3}a$, where a is the side size of a hexagon.

The following simple relations for the contributions E_0 to the total energy for GBs with misorientation angle θ in graphene can be proposed:

$$E_0 \cong \frac{md_Ae_A + nd_Be_B}{md_A + nd_B}, \quad 0^\circ < \theta < 21.8^\circ, \tag{6a}$$

$$E_0 \cong \frac{md_Be_B + nd_Ce_C}{md_B + nd_C}, \quad 21.8^\circ < \theta < 60^\circ, \tag{6b}$$

where interface energies per unit length $e_A = e_C = 0$ and $e_B = E_{5-7}$. Other designations are the same as in Eqs. (5a, b). Energy E_{5-7} is found from atomistic modelling.

As the final step the contributions $E_{elastic}$ and E_{core} are found with the help of analytical formulas of the disclination theory by considering a GB structure as the wall of the virtual disclination dipoles, see Ref. (Romanov et al. 2015) for detail.

Conclusions

We can conclude that the tools and techniques for the mesoscopic disclination description of IFs in graphene are effective both for determining the potential types of IFs and for calculating their elastic fields and energies. The continual theory of disclinations is especially effective in combination with atomistic modelling, when such parameters as the elastic moduli, IF period, etc. are found by MD simulation and used in the analytical formulas of the mesoscopic approach.

References

Avouris, P. (2010) Graphene: Electronic and photonic properties and devices. *Nano Letters*, 10 (11), 4285–4294. DOI: 10.1021/nl102824h (In English)

Bagri, A., Kim, S. P., Ruoff, R. S., Shenoy, V. B. (2011) Thermal transport across twin grain boundaries in polycrystalline graphene from nonequilibrium molecular dynamics simulations. *Nano Letters*, 11 (9), 3917–3921. DOI: 10.1021/nl202118d (In English)

Balandin, A. A., Ghosh, S., Bao, W. et al. (2008) Superior thermal conductivity of single-layer graphene. *Nano Letters*, 8 (3), 902–907. DOI: 10.1021/nl0731872 (In English)

Bravo, S., Correa, J., Chico, L., Pacheco, M. (2019) Symmetry-protected metallic and topological phases in penta-materials. *Scientific Reports*, 9, article 12754. DOI: 10.1038/s41598-019-49187-w (In English)

Castro Neto, A. H., Guinea, F., Peres, N. M. R. et al. (2009) The electronic properties of graphene. *Reviews of Modern Physics*, 81 (1), 109–162. DOI: 10.1103/RevModPhys.81.109 (In English)

Frank, I. W., Tanenbaum, D. M., van der Zande, A. M., McEuen, P. L. (2007) Mechanical properties of suspended graphene sheets. *Journal of Vacuum Science & Technology B: Microelectronics and Nanometer Structures Processing, Measurement, and Phenomena*, 25 (6), 2558–2561. DOI: 10.1116/1.2789446 (In English)

Geim, A. K., Novoselov, K. S. (2009) The rise of graphene. In: P. Rodgers (ed.). *Nanoscience and technology: A collection of reviews from nature journals*. London: Nature Publishing Group, pp. 11–19. DOI: 10.1142/9789814287005_0002 (In English)

Gertsman, V. V., Nazarov, A. A., Romanov, A. E. et al. (1989) Disclination-structural unit model of grain boundaries. *Philosophical Magazine A*, 59 (5), 1113–1118. DOI: 10.1080/01418618908209841 (In English)

Harris, W. F. (1977) Disclinations. *Scientific American*, 237 (6), 130–145.

Kolesnikova, A. L., Orlova, T. S., Hussainova, I., Romanov, A. E. (2014) Elastic models of defects in two-dimensional crystals. *Physics of the Solid State*, 56 (12), 2573–2579. DOI: 10.1134/S1063783414120166 (In English)

Kolesnikova, A. L., Romanov, A. E. (1998) A disclination-based approach to describing the structure of fullerenes. *Physics of the Solid State*, 40 (6), 1075–1077. DOI: 10.1134/1.1130490 (In English)

Kolesnikova, A. L., Rozhkov, M. A., Hussainova, I. et al. (2017) Structure and energy of intercrystallite boundaries in graphene. *Reviews on Advanced Materials Science*, 52, 91–98. (In English)

Kolesnikova, A. L., Rozhkov, M. A., Romanov, A. E. (2020) On fracture of pseudo-graphenes. *Mechanics of Solids*, 55 (1), 69–76. DOI: 10.3103/S0025654420010124 (In English)

Lee, Ch., Wei, X., Kysar, J. W., Hong, J. (2008) Measurement of the elastic properties and intrinsic strength of monolayer graphene. *Science*, 321 (5887), 385–388. DOI: 10.1126/science.1157996 (In English)

Nazarov, A. A., Romanov, A. E., Valiev, R. Z. (1993) On the structure, stress fields and energy of nonequilibrium grain boundaries. *Acta Metallurgica et Materialia*, 41 (4), 1033–1040. DOI: 10.1016/0956-7151(93)90152-I (In English)

Ovid'ko, I. A. (2013) Mechanical properties of graphene. *Reviews on Advanced Materials Science*, 34 (1), 1–11. (In English)

Romanov, A. E., Kolesnikova, A. L., Orlova, T. S. et al. (2015) Non-equilibrium grain boundaries with excess energy in graphene. *Carbon*, 81, 223–231. DOI: 10.1016/j.carbon.2014.09.053 (In English)

Romanov, A. E., Rozhkov, M. A., Kolesnikova, A. L. (2018) Disclinations in polycrystalline graphene and pseudo-graphenes. Review. *Letters on Materials*, 8 (4), 384–400. DOI: 10.22226/2410-3535-2018-4-384-400 (In English)

Romanov, A. E., Vladimirov, V. I. (1992) *Disclinations in crystalline solids.* In: F. R. N. Nabarro (ed.). *Dislocations in solid. Vol. 9: Dislocations and disclinations*. Amsterdam: North-Holland, pp. 191–402. (In English)

Rozhkov, M. A., Kolesnikova, A. L., Orlova, T. S. et al. (2016) Disclinated rings as structural units in MD simulation of intercrystallite boundaries in graphene. *Materials Physics and Mechanics*, 29 (1), 101–105. (In English)

Rozhkov, M. A., Kolesnikova, A. L., Yasnikov, I. S., Romanov, A. E. (2018) Disclination ensembles in graphene. *Low Temperature Physics*, 44 (9), 918–924. DOI: 10.1063/1.5052677 (In English)

Rozhkov, M. A., Kolesnikova, A. L., Hussainova, I. et al. (2018) Evolution of Dirac cone in disclinated graphene. *Reviews on Advanced Materials Science*, 57 (2), 137–142. DOI: 10.1515/rams-2018-0057 (In English)

Tang, Y., Mak, K. F., Shan, J. (2019) Long valley lifetime of dark excitons in single-layer WSe_2. *Nature Communication*, 10, article 4047. DOI: 10.1038/s41467-019-12129-1 (In English)

Wang, H., Huang, C.-C., Polcar, T. (2019) Triboelectrification of two-dimensional chemical vapor deposited WS_2 at nanoscale. *Scientific Reports*, 9, article 12570. DOI: 10.1038/s41598-019-49107-y (In English)

Zhang, J., Zhao, J. (2013) Structures and electronic properties of symmetric and nonsymmetric graphene grain boundaries. *Carbon*, 55 (1), 151–159. DOI: 10.1016/j.carbon.2012.12.021 (In English)

Condensed Matter Physics. Polymer Physics

UDC 538.9+537.3 DOI: 10.33910/2687-153X-2020-1-4-135-141

Molecular mobility in crystallising aromatic thermoplastic polyimide R-BAPS

N. A. Nikonorova✉[1], A. A. Kononov[2], R. A. Castro Arata[2]

[1] Institute of Macromolecular Compounds of Russian Academy of Sciences,
31 Bolshoy Ave., Saint Petersburg 199004, Russia
[2] Herzen State Pedagogical University of Russia, 48 Moika Emb., Saint Petersburg 191186, Russia

Authors

Natalia A. Nikonorova, ORCID: 0000-0002-7928-9227, e-mail: n_nikonorova2004@mail.ru

Alexey A. Kononov, ORCID: 0000-0002-5553-3782

Rene Alejandro Castro Arata, ORCID: 0000-0002-1902-5801

For citation: Nikonorova, N. A., Kononov, A. A., Castro Arata, R. A. (2020) Molecular mobility in crystallising aromatic thermoplastic polyimide R-BAPS. *Physics of Complex Systems*, 1 (4), 135–141. DOI: 10.33910/2687-153X-2020-1-4-135-141

Received 27 May 2020; reviewed 11 June 2020; accepted 11 June 2020.

Abstract. The molecular mobility of the thermoplastic aromatic *R-BAPS* polyimide films *based on 1,3-bis (3,3'-4,4'-dicarboxyphenoxy) benzene (dianhydride) and 4,4'-bis (4-aminophenoxy) biphenyl* was studied using the dielectric method. Two relaxation regions of dipole polarisation caused by local mobility of phenylene groups in the diamine (γ process) and in the diamine and dianhydride macromolecule parts (β process) were identified in the glassy state, In the high-elastic state, two relaxation processes, α and α_{MWS}, were also observed. The α process is due to the large-scale segmental mobility of macromolecules. The α_{MWS} process is caused by the relaxation at the boundary between amorphous and crystalline regions, i.e., the Maxwell-Wagner-Sillars relaxation. Moreover, a structural transition due to melting was observed in the initial samples.

Keywords: thermoplastic aromatic polyimide, molecular mobility, dielectric spectroscopy, relaxation time, glass transition temperature.

Introduction

Nowadays, well-developed synthesis methods make it possible to obtain polyimides (PI) with a very diverse chemical structure and molecular architecture and, consequently, with largely varied physical properties (Bryant 2002; Sroog 1969). There is a correlation between the polymer physical properties and the molecular mobility of the polar kinetic units. One of the methods to identify this correlation is dielectric spectroscopy. When the polymer system is studied by the dielectric method, the polar groups ("labels") reorientation causes the temperature-frequency dependences of the dielectric absorption regions. This provides information on the polymer molecular mobility at all molecular organisation levels. In turn, molecular motion properties depend on inter- and intramolecular interactions determined by the polymer chemical structure and morphological features (Hedvig 1977; Riande, Diaz-Calleja 2004). At least three relaxation regions of dipole polarisation—the γ, β and α processes—were detected using the dielectric spectroscopy for PIs with a largely varied chemical structure (Cheng et al. 1995; Chisca et al. 2011; Jacobs et al. 2010; Sun et al. 1992).

The research aim is to analyse the dielectric relaxation processes in the R-BAPS aromatic polyimide as well as to determine the molecular mobility mechanisms that cause dipole polarisation relaxations.

Experimental methods

The samples were thermoplastic polyimide films based on 1,3-bis- (3,3'-4,4'-dicarboxyphenoxy) benzene and 4,4'-bis- (4-aminophenoxy) biphenyl (R-BAPS) (Fig. 1) synthesised at the Institute

of Macromolecular Compounds, Russian Academy of Sciences (Smirnova et al. 2013; Svetlichnyi, Kudryavtsev 2003).

R-BAPS films were obtained from the 20% polyamide acid (PAA) solution, molecular weight Mw ~30,000 g/mol, dried at 60°C for 24 hours and subjected to stepwise heat treatment for 1 hour at 100°C, 200°C and 300°C (Kamalov et al. 2020; Yudin et al. 2002).

The dielectric spectra (frequency dependences of the dielectric loss factor, $\varepsilon'' = \phi(f)$) were obtained in the frequency range 10^{-1}–$3 \cdot 10^6$ Hz and temperatures –100–+400°C using the "Concept-21" broadband dielectric spectrometer (Novocontrol Technologies GmbH) with an ALPHA-ANB high-resolution automatic frequency analyser. The ~25–40 μm films were pressed between brass electrodes (the upper electrode was 20 mm in diameter) at a ~30°C higher temperature than the glass transition temperature. For the first measurement, the films were additionally warmed up to 250°C (the initial samples).

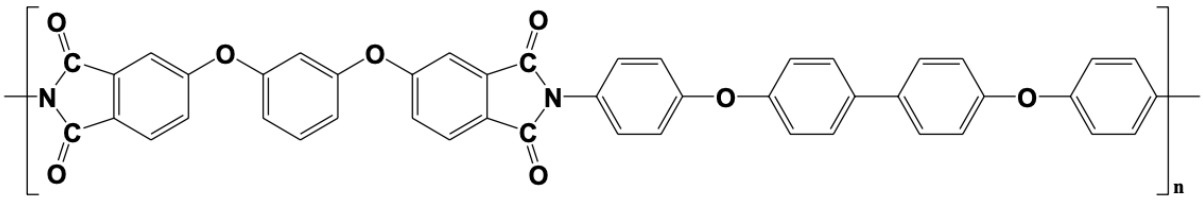

Fig. 1. The R-BAPS chemical formula

R-BAPS dielectric behaviour

The dielectric behaviour in the entire temperature range is shown in Fig. 2 which presents the temperature dependences of $tg\delta = \phi(T)$ for R-BAPS (for the initial sample) at various frequencies. Fig. 2 shows three $tg\delta_{max}$ regions: γ and β (in a glassy state) and α (in a highly elastic state) caused by the relaxation processes of the dipole polarisation, since the maximum temperature shifts towards high temperatures as frequency increases. A sharp increase in the dielectric loss and $tg\delta_{max}$ region due to the conductivity process was observed at temperatures exceeding the α process. Moreover, at 320°C there was a tgδ peak; the temperature did not change with frequency, while the intensity sharply decreased with frequency. This dielectric behaviour pattern is characteristic of a structural (non-relaxation) transition caused, in particular, by melting, which is confirmed by the DSC data (Kamalov et al. 2020). The tgδ peak at 320°C indicates a certain crystallinity of the initial sample. Heating the sample to 340°C (above the melting temperature) suppresses the structural transition at 320°C, as can be seen in the inset (Fig. 2).

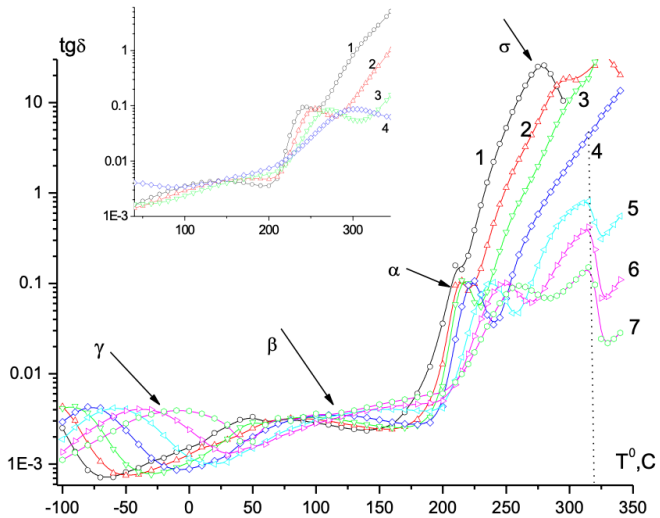

Fig. 2. The tgδ temperature dependences for R-BAPS at frequencies 0.1 (1), 1 (2), 10 (3), 100 (4), 1000 (5), 10000 (6) and 100000 (7) Hz, the initial measurement and the measurement after warming up to 340°C (inset)

DOI: 10.33910/2687-153X-2020-1-4-135-141

The dielectric spectra were analysed by describing the complex dielectric constant ε^* using the empirical Havriliak-Negami equation (HN), which, as a rule, reliably describes the dependences $\varepsilon'' = \phi(f)$ for various relaxation processes (Havriliak, Negami 1967):

$$\varepsilon^*(\omega) - \varepsilon_\infty = \sum_{k=1}^{n} \mathrm{Im}\left[\frac{\Delta\varepsilon_k}{\{1+(i\omega\tau_{HN_k})^{\alpha_k}\}^{\beta_k}}\right], \quad (1)$$

where $\varepsilon^* = \varepsilon'(\omega) - i\varepsilon''(\omega)$; $\omega = 2\pi f$ is the angular frequency; $\Delta\varepsilon = \varepsilon_0 - \varepsilon_\infty$ is the increment of the dielectric permittivity; τ_{HN} is the characteristic Havriliak-Negami relaxation time; α_{HN} and β_{HN} are the calculated parameters corresponding to the expansion and asymmetries of the relaxation time distribution, respectively, k is the number of the relaxation processes.

Above T_g, the contribution due to conductivity was taken into account in the formula (1): $\frac{\sigma_{dc} a}{\varepsilon_v \omega^s}$, where σ_{dc} is the direct current electrical conductivity, a is the constant, ε_v is the dielectric constant of the vacuum (Vallerien et al. 1989); τ_{max} was calculated by the following formula (Diaz-Calleja 2000):

$$\tau_{max} = \tau_{HN}\left[\frac{\sin\left(\frac{\pi(\alpha_{HN})\beta_{HN}}{2(\beta_{HN}+1)}\right)}{\sin\left(\frac{\pi(\alpha_{HN})}{2(\beta_{HN}+1)}\right)}\right]^{1/(\alpha_{HN})} \quad (2)$$

Fig. 3 shows the dielectric spectra for R-BAPS at various temperatures in the γ and β process regions, which are reliably described by a single HN process.

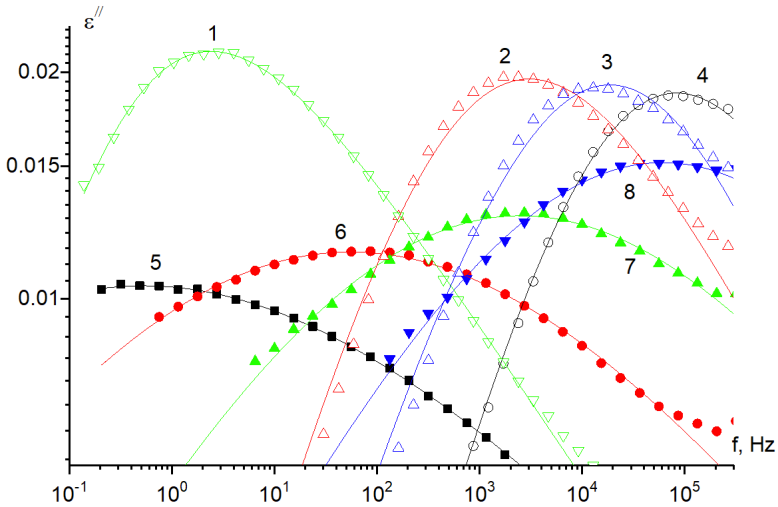

Fig. 3. The ε'' frequency dependences in the γ (1–4) and β (5–8) process regions for R-BAPS at –100°C (1), –80°C (2), –60°C (3), –10 °C (4), 60°C (5), 100°C (6), 140°C (7) and 180°C (8).
Symbols are experimental points. Continuous lines are the calculation according to the HN formula

In the highly elastic state, the polymer dielectric spectroscopy is usually described by the sum of two components—the α process and the contribution to the dielectric loss due to conductivity. In the case of the initial R-BAPS sample, the dielectric spectra in the 230–320°C temperature range can be described as the sum of three components: the α and α_{MWS} (at lower frequencies) relaxation processes and the contribution due to conductivity. Fig. 4 shows several dielectric spectra in a highly elastic state and a spectrum separation into three components.

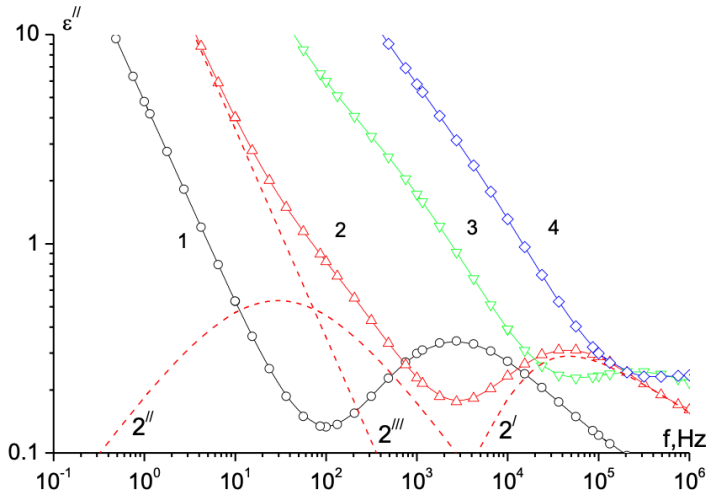

Fig. 4. The ε'' frequency dependences in the α and αMWS relaxation process regions for R-BAPS (the initial sample) at 240°C (1), 260°C (2), 280°C (3) and 300°C (4). Symbols are experimental points. Continuous lines are the description according to the HN formula. The dashed lines are the dielectric spectrum separation at 260°C into the α (2′) and αMWS processes (2″) and the contribution due to conductivity (2‴) according to the HN formula.

Despite the fact that the α_{MWS} process shows only a slight deviation from the linear increase in ε'' in the low frequencies / high temperatures (LF/HT) range, its allocation from the spectrum according to the HN formula is quite reliable, as shown in Fig. 5 (ε'' losses due to the conductivity are subtracted).

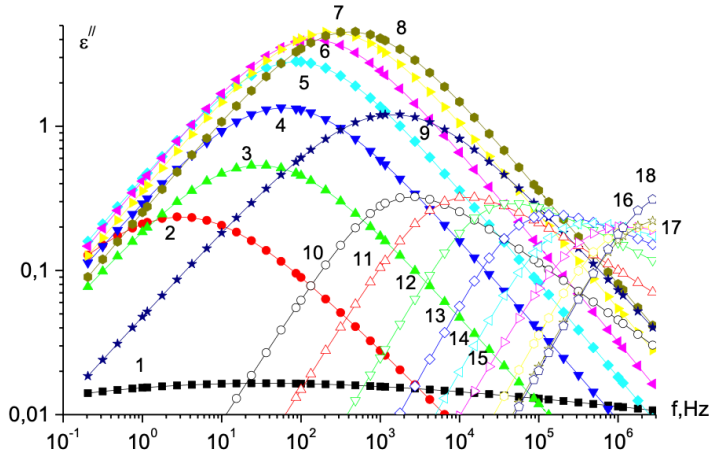

Fig. 5. The ε'' frequency dependences in the αMWS (1–9) and α (10–18) process regions for R-BAPS (the initial sample) at 240°C (1.10), 250°C (2.11), 260°C (3.12), 270°C (4.13), 280°C (5.14), 290°C (6.15), 300°C (7.16), 310°C (8.17) and 320°C (9.18)

The τ_{max} values calculated by the HN formula for R-BAPS (the initial sample) in the γ, β, α and α_{MWS} process regions are shown in Fig. 6, curves 1, 2, 3 and 5, respectively. After heating above 340°C, the relaxation region corresponding to the α_{MWS} process (curve 4) disappears; however, the relaxation time in the regions corresponding to the γ, β and α processes does not change.

For the γ, β and α_{MWS} processes, the $-log\tau_{max}$ dependencies on the inverse temperature are linear and are described by the Arrhenius equation:

$$\tau(T)_{max} = \tau_0 \exp\left(\frac{E_a}{RT}\right), \quad (3)$$

where $\tau_0 = \tau_{max}$ at $T \to \infty$, E_a is the activation energy, R is the universal gas constant.

DOI: 10.33910/2687-153X-2020-1-4-135-141

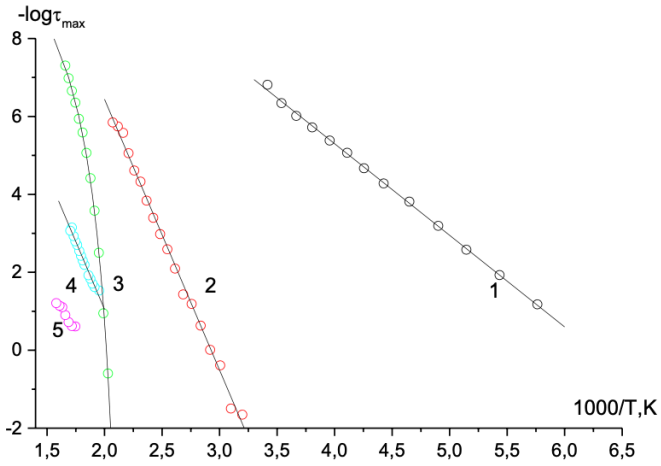

Fig. 6. The $-\log\tau_{max}$ dependencies on the inverse temperature for R-BAPS (the initial sample) for the γ (1), β (2), α (3), αMWS (4) and SCP (5) processes. τmax points are calculated using the HN formula. Curves describe the dependencies according to the formulas 3 (1, 2 and 5) and 4 (3)

The linear dependence $-log\tau_{max} = \phi(1/T)$ indicates that the activation energy does not depend on the temperature.

For the α process, the dependence $-log\tau_{max} = \phi(1/T)$ is curvilinear and is well described by the empirical Vogel-Tammann-Hesse (F-T-H) equation, which describes relaxation processes where the activation energy depends on the temperature (Donth 2001; Vogel 1921):

$$\tau_{max} = \tau_0 \exp(\frac{B}{T - T_0}) \quad (4),$$

where τ_0, B and T_0 are calculated parameters that do not depend on temperature (τ_0 is the pre-exponential factor, B is the activation parameter and T_0 is the so-called Vogel temperature).

Molecular mechanisms of dielectric processes

Three relaxation processes—the γ and β processes in the glassy state and the α process in the highly elastic state—were found for R-BAPS as well as for the previously studied PIs with different chemical structure (Cheng et al. 1995; Chisca et al. 2011; Jacobs et al. 2010; Nikonorova et al. 2019; Sun et al. 1992). Molecular mechanisms were proposed for the γ, β and α processes. It was believed that the γ process is caused by the local mobility of phenyl rings in the diamine part of the macromolecule as well as by the mobility of the bound water molecules (Chisca et al. 2011; Jacob et al. 2010). For the γ process, the relaxation time did not depend on the polymer structure, and the temperature $tg\delta_{max}$ was ~–100°C (at 1 Hz). For R-BAPS, the molecular source of the γ process is reorientation of the phenyl rings with the adjacent ether groups; therefore, the temperature $tg\delta_{max}$ was ~–100°C (at 1 Hz). The equation (3) parameters are given in Table 1.

Table 1. Parameters of equation 3 for γ, β and αMWS processes

	γ	β	α_{MWS}
$-lg\tau_0$	14.7	20.34	14.95
E_a, kcal/mol	10.8	10.8	31.9

It was suggested that the molecular mechanism of the β process corresponds to mobility in the dianhydride macromolecule part (Chisca et al. 2011), rotation of the para-phenylene units in the diamine part (Sun et al. 1992) and correlated local movements in both macromolecule parts (Chisca et al. 2011;

Jacobs et al. 2010; Sun et al. 1992). For the β process, the relaxation time depended on the sample chemical structure, thermal treatment and morphology, and the temperature $tg\delta_{max}$ was in the 50–150°C range (at 1 Hz). Based on the R-BAPS chemical structure, it can be assumed that the β process is related to the local movements of the phenyl rings in the diamine and dianhydride macromolecule parts with the adjacent ether and amide polar groups. In other words, the β process is the superposition of several molecular mobility modes with close relaxation times that cannot be separated. For R-BAPS, the temperature $tg\delta_{max}$ in the β process region was ~+75°C (at 1 Hz). The equation (3) parameters for the β process are given in Table 1.

The molecular source of the α process is the cooperative large-scale segmental mobility of a macromolecule related to the transition from the glassy to the highly elastic state. In this case, the temperature dependence $-\log\tau_{max}$ is usually nonlinear and the apparent activation energy varies depending on the temperature. In the α process region, the dependence $-\log\tau_{max} = \phi(1/T)$ separates the glassy state region (on the right) from the highly elastic state region (on the left). The equation (4) parameters $-\log\tau_0$, B and T_0 for the α process are 11.6 s, 1564 and 421 K, respectively. For R-BAPS, the temperature dependence of the relaxation time is shown by curve 3. The glass transition temperature of R-BAPS is 222°C. T_g was determined using the conventional dielectric method procedure—extrapolation of the $-\log\tau_{max} = \phi(1/T)$ dependence described by the F-T-H equation $\log\tau_{max} = 0$ ($\tau_{max} = 1$ s).

In polymers, a rapid increase in the dielectric loss is typically observed at temperatures above the α transition (in the highly elastic state) at HT / LF due to the space-charge polarisation (SCP). The SCP molecular source is the charges block on the electrode / sample surface which forms a double electric layer with large capacity that demonstrates huge values of ε', ε'' and tgδ. Moreover, the increment values of the dielectric permittivity (Δε) reach ~100...10 000 (Chisca et al. 2011; Lu et al. 2006; Neagu et al. 2000; Samet et al. 2015). The SCP effects are largely determined by the polymer purity (uncontrolled impurities, residual solvents and starting destruction of macromolecules in the polymer), rather than its chemical structure. Space-charge polarisation is considered a "parasitic" effect. During the polymer examination by the dielectric method, measures are taken to reduce it. The SCP temperature-frequency coordinates for R-BAPS are shown by curve 5 in Fig. 6, which is typical for this effect (Neagu et al. 2000; Samet et al. 2015).

Along with the SCP effect, polymers with heterogeneous structure—such as polymer mixtures, two-three-phase systems, nanocomposites and crystallising polymers—at HT / LF can demonstrate the Maxwell-Wagner-Sillars (MWS) polarisation, where the $-\log\tau_{max} = \phi(1/T)$ temperature dependence lies between the α process and the SCP effect (Chisca et al. 2011; Hedvig 1977; Klonos et al. 2017; Lu et al. 2006; Neagu et al. 2000; Samet et al. 2015; Tsonos et al. 2001). The MWS polarisation arises due to polarisation at the phase boundary when microphases of such systems have different conductivity and permittivity values. For R-BAPS, the α_{MWS} relaxation process, which is between the α process and the SCP effect, demonstrates several features. Firstly, this process takes place in the interval from T_g up to the melting temperature. Above 320°C it disappears, while the α process can be observed up to 350°C. Secondly, the Δε values of the α_{MWS} process are ~7–12. Thirdly, the $\lg\tau_{max} = \phi(1/T)$ dependence is linear (Fig, 6, curve 4, equation 3 parameters are given in the table), which is typical for the MWS polarisation (Klonos et al. 2017; Tsonos et al. 2001). These features suggest that the α_{MWS} relaxation process is caused precisely by the Maxwell-Wagner-Sillars polarisation in the initial P-BAPS samples where melting is observed. The molecular mechanism of the α_{MWS} process in R-BAPS is polarisation according to the MWS type at the boundary between the amorphous and the crystalline phases of the sample. This α_{MWS} process is observed only in crystallising samples and disappears in the amorphous sample after heating above 320°C. Annealing at 280°C, at which the R-BAPS crystalline phase is formed (Smirnova et al. 2013), causes the α_{MWS} process to reappear, i.e. this process is reproducible.

Conclusion

Thus, several relaxation regions of dipole polarisation, typical of the dielectric absorption pattern demonstrated by PIs with different structure, were identified by the dielectric method for aromatic thermoplastic PI R-BAPS in the –100–350°C temperature range. The dielectric spectra showed three maximum regions; these regions listed in order of increasing temperature are caused by local mobility in the diamine (the γ process) and joint movement in the diamine and dianhydride macromolecule parts (the β process), as well as the segmental cooperative mobility of macromolecules (the α process),

 DOI: 10.33910/2687-153X-2020-1-4-135-141

correspondingly. In a partially crystallised sample at temperatures exceeding the α process (at HT / LF), it was possible to see the α_{MWS} process which reflects the polarisation at the interface between the amorphous and crystalline phases, i.e., the MWS type polarisation. The difference in the sample dielectric behaviour is that in addition to the γ, β and α processes observed in the amorphous sample (warmed above 320°C), the partially crystalline (initial) sample also demonstrates the α_{MWS} process.

References

Bryant, R. G. (2002) Polyimides. In: H. F. Mark (ed.). *Encyclopedia of polymer science and technology. Vol. 7*. 4th ed. New York: John Wiley & Sons Publ., pp. 529–555. DOI: 10.1002/0471440264.pst272 (In English)

Cheng, S. Z. D., Chalmers, T. M., Gu, Y. et al. (1995) Relaxation processes and molecular motion in a new semicrystalline polyimide. *Macromolecular Chemistry and Physics*, 196 (5), 1439–1451. DOI: 10.1002/macp.1995.021960507 (In English)

Chisca, S., Musteata, V. E., Sava, I., Bruma, M. (2011) Dielectric behavior of some aromatic polyimide films. *European Polymer Journal*, 47 (5), 1186–1197. DOI: 10.1016/j.eurpolymj.2011.01.008 (In English)

Diaz-Calleja, R. (2000) Comment on the maximum in the loss permittivity for the Havriliak–Negami equation. *Macromolecules*, 33 (24), 8924–8924. DOI: 10.1021/ma991082i (In English)

Donth, E. (2001) *The glass transition: Relaxation dynamics in liquids and disordered materials. Vol. 48*. Berlin: Springer Science & Business Media Publ., 418 p. (In English)

Havriliak, S., Negami, S. (1967) A complex plane representation of dielectric and mechanical relaxation processes in some polymers. *Polymer*, 8, 161–210. DOI: 10.1016/0032-3861(67)90021-3 (In English)

Hedvig, P. (1977) *Dielectric spectroscopy of polymers*. Budapest: Akademiai Kiado, 312 p. (In English)

Jacobs, J. D., Arlen, M. J., Wang, D. H. et al. (2010) Dielectric characteristics of polyimide CP2. *Polymer*, 51 (14), 3139–3146. DOI: 10.1016/j.polymer.2010.04.072 (In English)

Kamalov, A. M., Borisova, M. E., Didenko, A. L. et al. (2020) Relaxation behavior of thermoplastic polyimide R-BAPB in the amorphous state. *Polymer Science. Series A*, 62 (2), 107–115. DOI: 10.1134/S0965545X20010058 (In English)

Klonos, P., Kyritsis, A., Bokobza, L. et al. (2017) Interfacial effects in PDMS/titania nanocomposites studied by thermal and dielectric techniques. *Colloids and Surfaces A: Physicochemical and Engineering Aspects*, 519, 212–222. DOI: 10.1016/j.colsurfa.2016.04.020 (In English)

Lu, H., Zhang, X., Zhang, H. (2006) Influence of the relaxation of Maxwell-Wagner-Sillars polarization and dc conductivity on the dielectric behaviors of nylon 1010. *Journal of Applied Physics*, 100 (5), article 054104. DOI: 10.1063/1.2336494 (In English)

Neagu, E., Pissis, P., Apekis, L. (2000) Electrical conductivity effects in polyethylene terephthalate films. *Journal of Applied Physics*, 87 (6), 2914–2922. DOI: 10.1063/1.372277 (In English)

Nikonorova, N. A., Kononov, A. A., Dao, H. T., Castro, R. A. (2019) Molecular mobility of thermoplastic aromatic polyimides studied by dielectric spectroscopy. *Journal of Non-Crystalline Solids*, 511, 109–114. DOI: 10.1016/j.jnoncrysol.2018.12.032 (In English)

Riande, E., Diaz-Calleja, R. (2004) *Electrical properties of polymers*. New York: Marcel Dekker Publ., 630 p. (In English)

Samet, M., Levchenko, V., Boiteux, G. et al. (2015) Electrode polarization vs. Maxwell-Wagner-Sillars interfacial polarization in dielectric spectra of materials: Characteristic frequencies and scaling laws. *The Journal of Chemical Physics*, 142 (19), article 194703. DOI: 10.1063/1.4919877 (In English)

Smirnova, V. E., Gofman, I. V., Ivan'kova, E. M. et al. (2013) Effect of single-walled carbon nanotubes and carbon nanofibers on the structure and mechanical properties of thermoplastic polyimide matrix films. *Polymer Science. Series A*, 55 (4), 268–278. DOI: 10.1134/S0965545X1304007X (In English)

Sroog, C. E. (1969) Polyimides. In: H. F. Mark, N. G. Gaylord, N. M. Bikales (eds.). *Encyclopedia of polymer science and technology. Vol. 11*. 1st ed. New York: John Wiley & Sons Publ., pp. 247–272. (In English)

Sun, Z., Dong, L., Zhuang, Y. et al. (1992) Beta relaxation in polyimides. *Polymer*, 33 (22), 4728–4731. DOI: 10.1016/0032-3861(92)90684-O (In English)

Svetlichnyi, V. M., Kudryavtsev, V. V. (2003) Polyimides and the problems of designing advanced structural composite materials. *Polymer Science. Series B*, 45 (5-6), 140–185. (In English)

Tsonos, C., Apekis, L., Viras, K. et al. (2001) Electrical and dielectric behavior in blends of polyurethane-based ionomers. *Solid State Ionics*, 143 (2), 229–249. DOI: 10.1016/S0167-2738(01)00858-X (In English)

Yudin, V. E., Svetlichnyi, V. M., Gubanova, G. N. et al. (2002) Semicrystalline polyimide matrices for composites: Crystallization and properties. *Journal of Applied Polymer Science*, 83 (13), 2873–2882. DOI: 10.1002/app.10277 (In English)

Vallerien, S. U., Kremer, F., Boeffel, C. (1989) Broadband dielectric spectroscopy on side group liquid crystal polymers. *Liquid Crystals*, 4 (1), 79–86. DOI: 10.1080/02678298908028960 (In English)

Vogel, H. (1921) The law of the relation between the viscosity of liquids and the temperature. *Physikalische Zeitschrift*, 22, 645–646. (In English)

Condensed Matter Physics. Physics of Transport Phenomena in Condensed Matter

UDC 538.935 DOI: 10.33910/2687-153X-2020-1-4-142-149

The calcium effect on the thermopower, critical temperature and charge-carrier system parameters in the $Y_{0.75-x}Ca_xPr_{0.25}Ba_2Cu_3O_y$ HTSC-system

E. V. Gasumyants[✉1, 2]

[1] Peter the Great St. Petersburg Polytechnic University, 29 Polytechnicheskaya Str., Saint-Petersburg 195251, Russia
[2] Herzen State Pedagogical University of Russia, 48 Moika Emb., Saint Petersburg 191186, Russia

Author

Vitaliy E. Gasumyants, ORCID: 0000-0002-5306-6738, e-mail: vgasum@yandex.ru

For citation: Gasumyants, V. E. (2020) The calcium effect on the thermopower, critical temperature and charge-carrier system parameters in the $Y_{0.75-x}Ca_xPr_{0.25}Ba_2Cu_3O_y$ HTSC-system. *Physics of Complex Systems*, 1 (4), 142–149. DOI: 10.33910/2687-153X-2020-1-4-142-149

Received 19 October 2020; reviewed 1 November 2020; accepted 1 November 2020.

Abstract. Superconducting properties and thermopower temperature dependences for two series of ceramic samples with $Y_{0.75-x}Ca_xPr_{0.25}Ba_2Cu_3O_y$ (x = 0–0.25) compositions are experimentally investigated. Thermopower temperature dependences are analysed using the phenomenological narrow-band model. The normal state energy spectrum and the charge-carrier system parameters including the Fermi level position are determined and the doping influence on their value is discussed. It is shown that the Fermi level position in $Y_{0.75-x}Ca_xPr_{0.25}Ba_2Cu_3O_y$ samples is determined by its pinning inside a local peak in the density-of-states function formed due to increasing calcium content. The influence of the observed normal-state energy spectrum modification on the critical temperature in the studied system is discussed.

Keywords: high-temperature superconductors, calcium doping, critical temperature, thermopower, narrow-band model, normal-state energy spectrum, Fermi level.

Introduction

The high-temperature superconductors (HTSC) were discovered more than 30 years ago; however, the electron pairing mechanism in these materials which results in anomaly high critical temperature values, T_c, is still not determined. Although different high-T_c superconductivity mechanisms have been proposed, none of them can be considered generally accepted. However, not only the superconducting properties of these materials seem unusual. Many HTSC properties not related directly to superconductivity and observable in the normal state are also not typical of standard objects in the solid state physics; for example, the electron transport phenomena. The characteristic temperature dependences of resistivity, ρ, thermopower, S, Hall, R_H and Nernst, Q, coefficients make it impossible to describe and quantitatively analyse them based on the classical electron transport models developed for metals or semiconductors (for early reviews, see Gasumyants 2001; Iye 1992; Kaiser, Ucher 1991; Ong 1990). It is obviously due to the structure of the normal-state energy spectrum in HTSC, but its main parameters remain to be not defined. This is why different models were suggested to explain the experimental results on the electron transport in HTSC-materials. One of them is the narrow-band model based on the assumption that the HTSC energy spectrum contains a narrow peak of the density-of-states function (Gasumyants et al. 1995). Unlike others, this model makes it possible to describe all the behaviour features of the four transport coefficients using a common parameter set with a clear physical meaning. It can be used to determine certain energy spectrum and charge-carrier system parameters by analysing the experimental results regarding the thermopower temperature dependences in samples of various composition, and thus to investigate the parameter modification depending on the doping type and level.

Studies on yttrium-based HTSC revealed the impurity that gives the system additional nontrivial properties not caused by other dopants. This impurity is calcium that replaces yttrium in the $YBa_2Cu_3O_y$ lattice (Jirak et al. 1988; Manthiram et al. 1988; Tokiwa et al. 1988). The effect of calcium doping on the T_c value depends on the initial sample composition. In the case of the close-to-stoichiometric $YBa_2Cu_3O_y$, calcium suppresses its superconductivity (Fisher et al. 1993; McCarron III et al. 1989; Parise, McCarron III 1989); however, in samples where the critical temperature was preliminary decreased by other factors (the oxygen deficit or the second introduced impurity), calcium can lead to the superconductivity restoration (Awana et al. 1996; Gasumyants et al. 1994; Gasumyants et al. 1998; Gasumyants, Elizarova, Vladimirskaya et al. 2000; Komarova et al. 2013; Liu et al. 1990; McCarron III et al. 1989; Martynova, Potapov et al. 2011; Parise, McCarron III 1989; Vladimirskaya et al. 1995). Besides, calcium doping makes the thermopower temperature dependences acquire additional properties (most pronounced in double-substituted systems) that are not observed if other substitutions are used (Elizarova, Gasumyants 1999; Gasumyants 2001; Gasumyants et al. 1998; Gasumyants, Elizarova, Patrina 2000; Ghorbani et al. 2003). Therefore, calcium-containing $YBa_2Cu_3O_y$ system samples are very intriguing objects to study.

This paper presents the results of the study of the calcium doping effect on the critical temperature value and the thermopower behaviour in $Y_{0.75-x}Ca_xPr_{0.25}Ba_2Cu_3O_y$ samples.

Samples and experiment

Ceramic samples with $Y_{0.75-x}Ca_xPr_{0.25}Ba_2Cu_3O_y$ (x = 0–0.25) compositions were prepared by the standard solid-state technique from initial oxides or carbonates with purity higher than 99%. Their synthesis included three stages with intermediate regrinding and was performed in air. Thus, the initial sample series (series 1) was made. In order to obtain more extensive information on the calcium doping effect, we also studied an additional sample series of the same cation compositions that differs in conditions of the oxygen subsystem. Samples in this series (series 2) had maximum oxygen saturation due to their additional annealing in oxygen flow at T = 450°C for 2 h.

X-ray diffraction analysis showed that all the samples were almost single phase with foreign impurities not exceeding 1–2 %. The sample homogeneity was controlled by measuring the thermopower local values in various points on the sample surface at room temperature.

The resistivity and the thermopower were measured in the $T = T_c$–300 K temperature range. For resistivity measurements, the standard four-probe low-frequency ac (f = 20 Hz) method was used. The thermopower was measured by a differential method relative to copper electrodes at the temperature difference between the two ends of a sample about 2 K and then calculated by correction for the absolute copper thermopower. The measurement error for both transport coefficients did not exceed 5%.

Experimental results

The ρ(T) dependences for all the studied samples demonstrate a T-linear resistivity decrease with decreasing temperature in the whole measured temperature range that is typical of most $YBa_2Cu_3O_y$ system HTSC samples, excluding very strong doping cases (Gasumyants 2001; Kaiser, Ucher 1991). The critical temperature values determined by the resistive measurements are shown in Figure 1.

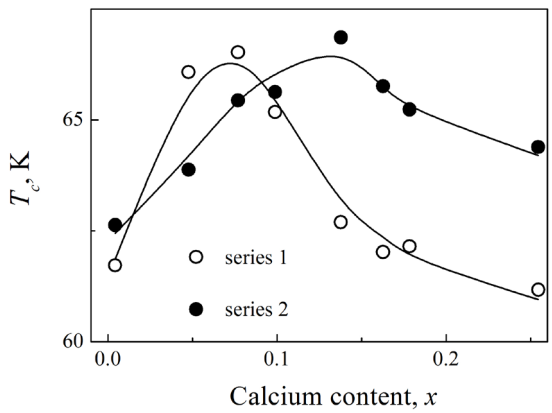

Fig. 1. Critical temperature vs. calcium content in $Y_{0.75-x}Ca_xPr_{0.25}Ba_2Cu_3O_y$ samples

The $T_c(x)$ dependences for both studied samples series are non-monotonic. When the calcium content is low, the critical temperature increases, but it starts to decrease with further increase in x. Besides, the position of the maximum on the $T_c(x)$ curve depends on the oxygen subsystem condition. For series 2 with a higher oxygen content, this maximum moves to a higher calcium doping level.

The $S(T)$ dependences measured for series 2 are shown in Figure 2. They are typical for calcium-containing samples of the $YBa_2Cu_3O_y$ system. The thermopower demonstrates a maximum at a temperature well above T_c whose position depends on the specific calcium content. Further increase in temperature results in a linear thermopower decrease. It should be noted that the latter is the distinguishing feature of the thermopower behaviour when calcium ions are present in the $YBa_2Cu_3O_y$ lattice (as for other impurities, the thermopower becomes almost temperature-independent at high temperatures) (Gasumyants, Martynova 2017). Nevertheless, there is an additional characteristic feature in the $S(T)$ modification under calcium doping in the studied system. In most systems, increased calcium content causes a T-linear region to appear on the $S(T)$ curve and results in a gradual increase in the $S(T)$ slope (Gasumyants, Martynova 2017). As seen in Figure 2, the $S(T)$ slope in the $Y_{0.75-x}Ca_xPr_{0.25}Ba_2Cu_3O_y$ system remains almost unchanged. This indirectly confirms our earlier conclusion that, if Ca and Pr are simultaneously introduced into the lattice, their influence on the $YBa_2Cu_3O_y$ properties cannot be considered a simple summation of their individual influences because calcium and praseodymium ions interact with each other (Martynova, Gasumyants 2006; Martynova, Gasumyants, Babichev 2011).

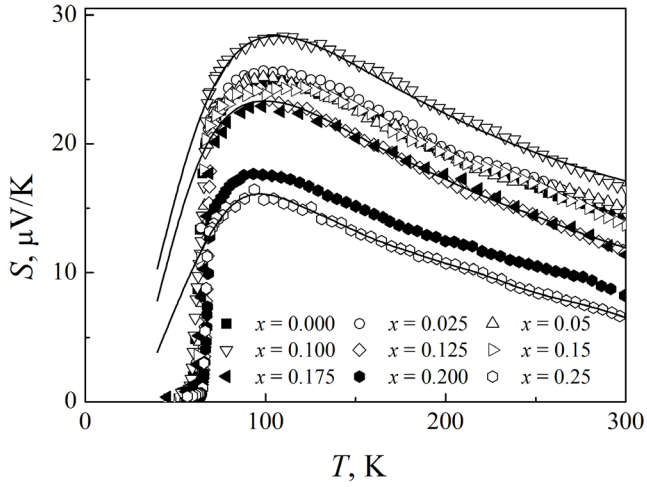

Fig. 2. Thermopower temperature dependences in oxygen-saturated $Y_{0.75-x}Ca_xPr_{0.25}Ba_2Cu_3O_y$ samples (series 2). Symbols are the experimental data; lines are the calculation results according to the narrow-band model

Series 1 experimental $S(T)$ dependences are analogous in quality to those of series 2, and thus demonstrate all the properties described above. The only difference is the absolute thermopower value. Since the oxygen deficit is known to result in increased thermopower value, the S values at T = 300 K change from 6.6 to 16.4 mV/K for series 2 and from 14.2 to 20.3 mV/K for series 1.

Discussion

The experimental $S(T)$ dependences were analysed within the narrow-band model (for the detailed model description see Gasumyants et al. 1995). Briefly, this approach is based on the assumption that the HTSC energy spectrum contains a single narrow band responsible for the conduction process or a sharp peak in the density-of-states function located near the Fermi level position. In this case, the simplest rectangular approximations can be used for the density-of-states, $D(\varepsilon)$, differential conductivity, $\sigma(\varepsilon)$, and Hall conductivity functions. Due to both the energy dependence character of these functions and a possible charge-carriers localisation at the band edges, the approximating rectangles should have rather different widths (Gasumyants et al. 1995). Besides, taking into account a possible $D(\varepsilon)$ function asymmetry, the centres of rectangles approximating the $D(\varepsilon)$ and $\sigma(\varepsilon)$ functions should be shifted relative to each other. Within such approximations, the energy structure of the narrow conduction band is characterised by three parameters — W_D is the total effective bandwidth, W_σ is the effective width of the delocalised states interval and b is the band asymmetry degree. The fourth needed

 DOI: 10.33910/2687-153X-2020-1-4-142-149

parameter is the band filling with electrons determined as $F = n/N$, where n is the total number of electrons in the band and N is the total number of the band states.

Based on the model-independent kinetic integrals and the above approximations for the $D(\varepsilon)$ and $\sigma(\varepsilon)$ functions, the following analytical expression is easily derived for the thermopower temperature dependence:

$$S = -\frac{k_B}{e}\left\{\frac{W_\sigma^*}{\sinh W_\sigma^*}\left[\exp\left(-\mu^*\right)+\cosh W_\sigma^* - \frac{1}{W_\sigma^*}\left(\cosh\mu^* + \cosh W_\sigma^*\right)\ln\frac{\exp\left(\mu^*\right)+\exp\left(W_\sigma^*\right)}{\exp\left(\mu^*\right)+\exp\left(-W_\sigma^*\right)}\right] - \mu^*\right\},$$

where:

$$\mu^* \equiv \mu / k_B T = \ln\frac{\sinh\left(FW_D^*\right)}{\sinh\left[\left(1-F\right)W_D^*\right)]} - 2bW_D^*,$$

$W_D^* \equiv \dfrac{W_D}{2k_B T}$, $W_\sigma^* \equiv \dfrac{W_\sigma}{2k_B T}$, k_B is the Boltzmann constant, e is the elementary change, μ is the electrochemical potential.

As shown by Gasumyants (2001) and Gasumyants et al. (1995), it is possible to obtain the calculated curves that describe the thermopower behaviour for HTSC samples with varied composition using different model parameter values in the above formulae. Fitting the experimental $S(T)$ curves obtained for different samples into the above equation determines the model parameter values characterising the energy spectrum structure in each sample.

The described approach was used to analyse the experimental results and allowed us to achieve a good agreement between the experimental and calculated $S(T)$ dependences for all the studied samples. To illustrate this agreement, several calculated $S(T)$ curves are shown in Figure 2 together with the experimental results. The observed variations in the energy spectrum and charge-carrier system parameters in the $Y_{0.75-x}Ca_xPr_{0.25}Ba_2Cu_3O_y$ system with increasing calcium content are discussed below.

Firstly, the band asymmetry degree for studied samples in series 1 and 2 with the same calcium content is almost equal. As the calcium content increases, the b value changes linearly and the $b(x)$ dependence corresponds very well to the $b \approx -0.12 \cdot x$ relationship characteristic of other yttrium system calcium-containing samples (Gasumyants, Elizarova, Vladimirskaya et al. 2000; Gasumyants, Martynova 2017). Obviously, this is because it is calcium that causes the band asymmetry in $YBa_2Cu_3O_y$ to appear due to additional states introduced into the conduction band.

Figure 3 shows the effective conduction bandwidth variation in two $Y_{0.75-x}Ca_xPr_{0.25}Ba_2Cu_3O_y$ sample series. It shows that the bandwidth decreases almost linearly as the calcium content increases, and the W_D value for samples in series 1 are always higher that for corresponding samples in series 2. Contrary to the studied system, if there is a single Ca→Y substitution in the $YBa_2Cu_3O_y$ system, calcium doping results in a slight band broadening (Gasumyants 2001; Gasumyants, Martynova 2017). To explain the obtained results, it is necessary to take into account the following. Firstly, single praseodymium doping leads to a strong increase in the W_D value due to hybridisation of Pr ion and band states

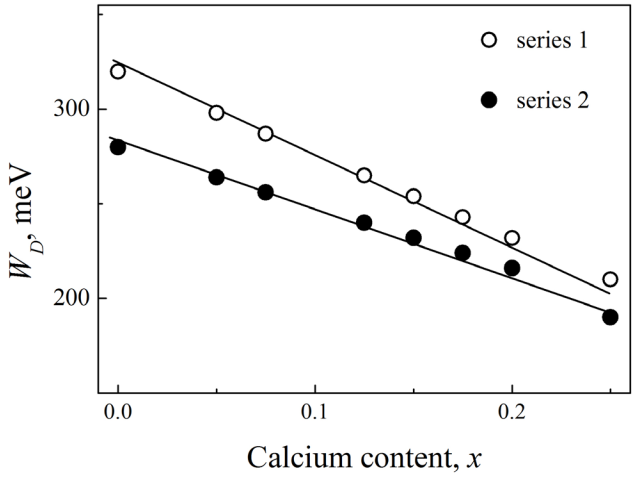

Fig. 3. Effective bandwidth vs. calcium content in $Y_{0.75-x}Ca_xPr_{0.25}Ba_2Cu_3O_y$ samples

(Gasumyants et al. 1997) that results in high W_D values for initial samples in both series. Secondly, increasing oxygen deficit also leads to the W_D rise, hence higher bandwidth values in series 1. Thirdly, as mentioned earlier, Ca and Pr ions interact when simultaneously introduced into the lattice. As a result, the Pr effect on the band structure gradually weakens as calcium content increases, causing the observed band narrowing in the studied system. Thus, the obtained $W_D(x)$ dependences can be explained consistently taking into account the specific features of the influence of the studied impurities on the energy spectrum structure.

Figure 4 shows the variation of the band filling with electrons in two $Y_{0.75-x}Ca_xPr_{0.25}Ba_2Cu_3O_y$ sample series. In general, the $F(x)$ dependences for both sample series demonstrate a tendency to a linear decrease. This is characteristic of calcium doping because it increases the total number of states in the band by introducing additional states, and therefore decreases the degree to which it is filled with electrons (Gasumyants, Elizarova, Vladimirskaya 2000; Gasumyants, Martynova 2017). However, the $F(x)$ dependence in both sample series reaches a plateau at x = 0.125–0.15 for oxygen-deficient samples and x = 0.075–0.175 for oxygen-saturated ones. In order to clarify the reason underlying this fact, it seems reasonable to analyse the Fermi level movement in the studied systems.

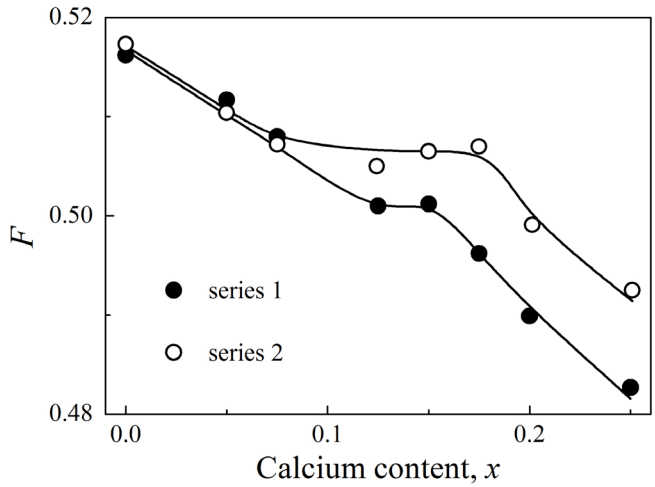

Fig. 4. The band filling with electrons vs. calcium content in $Y_{0.75-x}Ca_xPr_{0.25}Ba_2Cu_3O_y$ samples

According to our analysis (Komarova, Gasumyants 2010), the low-temperature Fermi level position relative to the middle of the conduction band can be calculated as $E_F = (F - ½)W_D - bW_D$. Calculation results are shown in Figure 5. The Fermi level remains almost constant in a wide calcium doping range, namely, at x = 0–0.2 and x = 0–0.175 for oxygen-deficient and oxygen-saturated series, respectively. As mentioned earlier, calcium ions form an additional peak in the $D(\varepsilon)$ function. Two investigated sample series differ very slightly in the oxygen content; therefore, we can suppose that for the initial samples in both series the Fermi level is located in the energy range where the local calcium peak in the $D(\varepsilon)$ function will be formed. If so, since a calcium-induced peak becomes more pronounced as x increases, the Fermi level is pinned inside this peak. When calcium content is high, E_F moves outside this peak and shifts to lower energies. A minor difference in calcium content at which the pinning effect is observed in different sample series is explained by the influence of the slightly changing oxygen content on the starting (in calcium-free samples) Fermi level position in these two series. It should be noted that the Fermi level in the pinning range (4–6 meV, see Fig. 5) corresponds well to our previously drown conclusion that calcium-induced peak is located in the energy range 2–8 meV from the band middle (Komarova et al. 2013).

Thus, we can conclude that such properties as absolute thermopower and critical temperature values should be influenced by the Fermi level pinning inside the forming calcium-induced peak in the density-of-states function.

Finally, let us discuss the critical temperature variation in the investigated system. According to our previous results, the critical temperature in doped $YBa_2Cu_3O_y$ is always affected by changes in the density-of-states function value at the Fermi level, $D(E_F)$. The main reason for these changes is

 DOI: 10.33910/2687-153X-2020-1-4-142-149

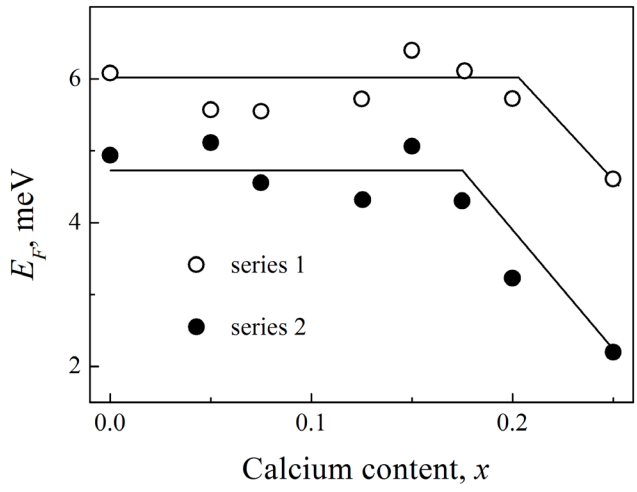

Fig. 5. Fermi level position vs. calcium content in $Y_{0.75-x}Ca_xPr_{0.25}Ba_2Cu_3O_y$ samples

an impurity-induced variation of the conduction band width. It is confirmed by the fact that T_c and W_D in doped $YBa_2Cu_3O_y$ samples for most doping types fall well on the universal $T_c(W_D)$ correlation dependence (Gasumyants 2001). However, in general, the $D(E_F)$ value in doped samples can be affected by several factors. In the $Y_{0.75-x}Ca_xPr_{0.25}Ba_2Cu_3O_y$ system, it is necessary to take into account the following possible reasons for the $D(E_F)$ change: (1) the energy spectrum modification induced by the Pr introduction into the lattice; (2) Pr and Ca ions interaction; (3) the direct calcium effect on the energy spectrum structure, i.e., the formation of the Ca-induced peak in the $D(\varepsilon)$ function; (4) the Fermi level position variation under doping including the effect of E_F pinning inside the forming Ca-induced peak. Clearly, it is rather impossible to estimate quantitatively the resultant effect of all these factors have on the $D(E_F)$ value and, therefore, on the critical temperature. However, it is necessary to consider that the peak positions on the $T_c(x)$ dependence in both investigated sample series correspond to the calcium content range in which the Fermi level pinning effect is observed. Therefore, it is possible to suppose that this is the $D(E_F)$ variation under calcium doping that results in the observed complicated $T_c(x)$ dependences in the $Y_{0.75-x}Ca_xPr_{0.25}Ba_2Cu_3O_y$ system.

Conclusions

This paper presents the experimental study results on the thermopower in two series of $Y_{0.75-x}Ca_xPr_{0.25}Ba_2Cu_3O_y$ samples with different oxygen subsystem conditions and their quantitative analysis using the narrow-band model. The obtained results and conclusions can be summarised as follows.

1) The critical temperature in the $Y_{0.75-x}Ca_xPr_{0.25}Ba_2Cu_3O_y$ system changes insignificantly and non-monotonically as the calcium content increases and its maximum position depends on the oxygen subsystem condition in the corresponding sample series.
2) Contrary to other calcium-containing systems, increased calcium content in the $Y_{0.75-x}Ca_xPr_{0.25}Ba_2Cu_3O_y$ system does not lead to a rise in the $S(T)$ slope and leads to a narrowing of the band responsible for the conduction process. Both these effects can be associated with praseodymium and calcium ions interaction that weakens hybridisation of the praseodymium and band states.
3) The Fermi level position variation in the $Y_{0.75-x}Ca_xPr_{0.25}Ba_2Cu_3O_y$ samples is related to its pinning inside the local calcium-induced peak in the density-of-states function formed as the calcium content increases.
4) Although several factors affect the value of the density-of-states function at the Fermi level in the $Y_{0.75-x}Ca_xPr_{0.25}Ba_2Cu_3O_y$ system, the observed variations in the critical temperature are determined by the $D(E_F)$ change under doping and can be explained by doping-induced modification of the normal-state energy spectrum under the Fermi level pinning effect.

References

Awana, V. P. S., Malik, S. K., Yelon, W. B. (1996) Structural aspects and superconductivity in oxygen-deficient $Y_{1-x}Ca_xBa_2Cu_3O_{7-y}$ ($y \approx 0.3$) systems A neutron-diffraction study. *Physica C: Superconductivity*, 262 (3-4), 272–278. DOI: 10.1016/0921-4534(96)00213-4 (In English)

Elizarova, M. V., Gasumyants, V. É. (1999) Superconductivity, Seebeck coefficient, and band structure transformation in $Y_{1-x}Ca_xBa_2Cu_{3-x}Co_xO_y$ ($x = 0–0.3$). *Physics of the Solid State*, 41 (8), 1248–1255. DOI: 10.1134/1.1130976 (In English)

Fisher, B., Genossar, J., Kuper, C. G. et al. (1993) Effects of substituting calcium for yttrium on the properties of $YBa_2Cu_3O_{7-\delta}$. *Physical Review B*, 47 (10), 6054–6059. DOI: 10.1103/PhysRevB.47.6054 (In English)

Gasumyants, V. E. (2001) Analysis of the electron transport phenomena in HTSC-materials as the method of studying the band spectrum and its transformation under doping by different impurities. In: F. Gerard (ed.). *Advances in condensed matter and materials research. Vol. 1.* New York: Nova Science Publ., pp. 135–200. (In English)

Gasumyants, V. E., Elizarova, M. V., Patrina, I. B. (2000) Thermoelectric power and band spectrum transformation in $Y_{1-x}Ca_xBa_{2-x}La_xCu_3O_y$. *Superconductor Science and Technology*, 13 (12), 1600–1606. DOI: 10.1088/0953-2048/13/12/306 (In English)

Gasumyants, V. E., Elizarova, M. V., Vladimirskaya, E. V., Patrina, I. B. (2000) Ca effect on the normal-state and superconducting properties of Y-based HTS. *Physica C: Superconductivity*, 341–348, pt 1, 585–588. DOI: 10.1016/S0921-4534(00)00604-3 (In English)

Gasumyants, V. E., Kaidanov, V. I., Vladimirskaya, E. V. (1995) The electron transport phenomena in Y-based HTSC's and their analysis on the basis of phenomenological narrow-band theory. The band structure transformation with oxygen content and substitution for Cu. *Physica C: Superconductivity*, 248 (3-4), 255–275. DOI: 10.1016/0921-4534(95)00173-5 (In English)

Gasumyants, V. E., Martynova, O. A. (2017) Chapter 4. Specific features of the thermopower behavior of calcium-containing Y-based high-temperature superconductors: Experimental investigation and interpretation. In: A. Reimer (ed.). *Horizons in world physics. Vol. 291.* New York: Nova Science Publ. pp. 129–216. (In English)

Gasumyants, V. É., Vladimirskaya, E. V., Elizarova, M. V., Ageev, N. V. (1998) The possibility of introducing additional states in the conduction band of $YBa_2Cu_3O_y$ by Ca doping. *Physics of the Solid State*, 40 (12), 1943–1949. DOI: 10.1134/1.1130710 (In English)

Gasumyants, V. E., Vladimirskaya, E. V. Patrina, I. B. (1997) Analysis of the possible reasons for the suppression of superconductivity in the $Y_{1-x}Pr_xBa_2Cu_3O_y$ system on the basis of thermoelectric power data. *Physics of the Solid State*, 39 (9), 1352–1357. DOI: 10.1134/1.1130077 (In English)

Gasumyants, V. E., Vladimirskaya, E. V., Patrina, I. B. (1994) Transport properties, band spectrum, and superconductivity in the $Y_{1-x}Ca_xBa_2Cu_{3-y}Co_yO$ system. *Physica C: Superconductivity*, 235–240, pt 2, 1467–1468. DOI: 10.1016/0921-4534(94)91958-5 (In English)

Ghorbani, S. R., Andersson, M., Rapp, Ö. (2003) Normal state Hall effect in $Nd_{1-x}Ca_xBa_2Cu_3O_{7-\delta}$: Competition between added charge and disorder. *Physica C: Superconductivity*, 390 (2), 160–166. DOI: 10.1016/S0921-4534(03)00700-7 (In English)

Iye, Y. (1992) Transport properties of high T_c cuprates. In: D. M. Ginsberg (ed.). *Physical properties of high temperature superconductors III.* Singapore: World Scientific Publ., pp. 285–361. DOI: 10.1142/9789814439688_0004 (In English)

Jirák, Z., Hejtmánek, J., Pollert, E. et al. (1988) Structure and superconductivity in $Y_{1-x}Ca_xBa_2Cu_3O_7$. *Physica C: Superconductivity*, 156 (5), 750–754. DOI: 10.1016/0921-4534(88)90153-0 (In English)

Kaiser, A. B., Ucher, C. (1991) Thermoelectrisity of high-temperature superconductors. In: A. V. Narlikar (ed.). *Studies of high temperature: Superconductors advances in research and applications. Vol. 7*. New York: Nova Science Publ., pp. 353–392. (In English)

Komarova, O. S., Gasumyants, V. E. (2010) Determination of the parameters of the normal state in doped yttrium high-temperature superconductors from thermopower coefficients in terms of different models of electron transport. *Physics of the Solid State*, 52 (4), 671–679. DOI: 10.1134/S1063783410040013 (In English)

Komarova, O. S., Martynova, O. A., Gasumyants, V. E. (2013) Doping-induced variations of the Fermi level in calcium-containing Y-based HTSC and their influence on the critical temperature. *Physica C: Superconductivity*, 495, 19–24. DOI: 10.1016/j.physc.2013.07.010 (In English)

Liu, R. S., Cooper, J. R., Loram, J. W. et al. (1990) Induced superconductivity in tetragonal $YBa_2Cu_3O_6$ by incorporation of Ca. *Solid State Communications*, 76 (5), 679–683. DOI: 10.1016/0038-1098(90)90115-R (In English)

Manthiram, A., Lee, S.-J., Goodenough, J. B. (1988) Influence of Ca on superconductivity of $Y_{1-x}Ca_xBa_2Cu_3O_{7-\delta}$. *Journal of Solid State Chemistry*, 73 (1), 278–282. DOI: 10.1016/0022-4596(88)90080-1 (In English)

Martynova, O. A., Gasumyants, V. É. (2006) Mechanism governing modification of the properties of the normal state and the critical temperatures under codoping of $YBa_2Cu_3O_y$ by calcium and praseodymium. *Physics of the Solid State*, 48 (7), 1223–1229. DOI: 10.1134/S106378340607002X (In English)

Martynova, O. A., Gasumyants, V. E., Babichev, A. V. (2011) Specific features of praseodymium-doping induced changes in the critical temperature and energy spectrum parameters of $YBa_2Cu_3O_y$ in the presence of calcium ions in the lattice. *Physics of the Solid State*, 53 (9), article 1769. DOI: 10.1134/S1063783411090198 (In English)

Martynova, O. A., Potapov, D. V., Gasumyants, V. E., Vladimirskaya, E. V. (2011) Mechanism of a strong rise of T_c due to the calcium doping in $Y_{1-x}Ca_xBa_2Cu_{2.8}Zn_{0.2}O_y$. *Physica C: Superconductivity*, 471 (9-10), 308–313. DOI: 10.1016/j.physc.2011.02.011 (In English)

McCarron III, E. M., Crawford, M. K., Parise, J. B. (1989) Observation of superconductivity in $(Y_{1-x}Ca_x)Ba_2Cu_3O_6$. *Journal of Solid State Chemistry*, 78 (1), 192–196. DOI: 10.1016/0022-4596(89)90145-X (In English)

Ong, N. P. (1990) The Hall effect and its relation to other transport phenomena in the normal state of the high-temperature superconductors. In: D. M. Ginsberg (ed.). *Physical properties of high temperature superconductors II.* Singapore: World Scientific Publ., pp. 459–508. (In English)

Parise, J. B., McCarron III, E. M. (1989) The structure of the 44 K superconductor $(Y_{1-x}Ca_x)Ba_2Cu_3O_{6+\delta}$ ($\delta \leq 0.2$). *Journal of Solid State Chemistry*, 83 (1), 188–197. DOI: 10.1016/0022-4596(89)90068-6 (In English)

Tokiwa, A., Syono, Y., Kikuchi, M. et al. (1988) Crystal structure and superconductivity controlled by cation substitution and oxygen annealing in $Y_{1-x}Ca_xBa_2Cu_3O_y$ and $YBa_{2-x}La_xCu_3O_y$. *Japanese Journal of Applied Physics*, 27 (6A), article L1009. DOI: 10.1143/JJAP.27.L1009 (In English)

Vladimirskaya, E. V., Gasumyants, V. E., Patrina, I. B. (1995) Influence of double substitutions on transport properties, superconductivity, and band spectrum in the $YBa_2Cu_3O_y$ system. *Physics of the Solid State*, 37 (7), 1084–1087. (In English)

Theoretical Physics. Quantum Field Theory

UDC 530.182 DOI: 10.33910/2687-153X-2020-1-4-150-157

Linear properties of chaotic states of systems described by equations of nonlinear dynamics: Analogy with quantum theory

A. V. Liaptsev✉[1]

[1] Herzen State Pedagogical University of Russia, 48 Moika Emb., Saint Petersburg 191186, Russia

Author

Alexander V. Liaptsev, ORCID: 0000-0002-8702-9062, e-mail: Lav@herzen.spb.ru

For citation: Liaptsev, A. V. (2020) Linear properties of chaotic states of systems described by equations of nonlinear dynamics: Analogy with quantum theory. *Physics of Complex Systems*, 1 (4), 150–157.
DOI: 10.33910/2687-153X-2020-1-4-150-157

Received 10 October 2020; reviewed 3 November 2020; accepted 3 November 2020.

Abstract. The paper provides a theoretical exploration of properties of systems described by equations of nonlinear dynamics in a chaotic state. Using the example of a system described by Duffing equations, it is shown that when the state of the system corresponds to a chaotic (strange) attractor, it is possible to determine a function whose meaning corresponds to the probability density. In this case, the resulting equation for the probability density is linear, so that the solution methods developed for linear differential equations, in particular the method of perturbation theory, can be applied to solve the equation in question. This results in a linear dependence of the average values of physical quantities on the parameter that characterizes small perturbations of the system. The numerical experiment confirms this linear relationship.

Keywords: nonlinear dynamics, strange attractor, probability density, chaos, perturbation theory.

Introduction

The specific properties of systems described by nonlinear equations have been known for a long time. One of the first works performed in the 19th century is the observation of solitons—solitary waves on the surface of water, as well as the study of the corresponding solutions of the Korteweg—de Vries equation. Currently, there are independent fields of study that focus on nonlinear waves and signals, such as nonlinear optics and nonlinear dynamics. Today, these fields of study develop largely due to the capabilities of modern computer technology, since it is the combination of analytical and computational research methods that allows us to advance in elucidating the qualitative features inherent in these phenomena. An overview of recent developments in the field of nonlinear dynamics can be found in (Gonchenko et al. 2017; Loskutov 2007). It should also be noted that the availability of sufficiently powerful computers and appropriate software allows us to set tasks related to non-linear systems as educational tasks at universities and even at school.

A characteristic feature of the system described by nonlinear equations is the occurrence of chaos at certain parameters of the system. Despite the determinism of solutions of the equations of classical dynamics, the nonlinearity of these equations leads to the fact that the state of the dynamical system is unpredictable after a characteristic time that determines the horizon of predictability. As noted by G. M. Zaslavsky and R. Z. Sagdeev in one of the first monographs on this topic (Sagdeev et al. 1988), since the trajectories of particles in phase space become in this case extremely complex and confusing, it is useless to monitor each trajectory separately. Instead, one should consider a set of trajectories that at any time occupy a finite volume of phase space, and the distribution of particles in it is characterized by some density.

Calculation of the probability density is a standard problem in statistical physics and quantum mechanics. It should be noted that the equations of quantum theory are linear. This leads to the fact that the evolution of a quantum mechanical system is in a certain sense deterministic. Naturally, this determinism is different from what occurs in classical dynamics. Solutions of the equations do not make it possible to predict at what point in the phase space the system is located at some point in time. However, solving the equations makes it possible to determine the probability that the system under consideration is located in a given region of the phase space at a given time.

The question arises whether it is possible for systems described by classical dynamical equations whose solutions correspond to a chaotic state to formulate equations that determine the probability density, similar to the equations in quantum theory and statistical physics. It turns out that this can be done, at least for the simplest systems. Similar equations were obtained for a rotator in an external harmonic field (Liapzev 2019). Numerical experiments show that solving equations for the probability density gives similar results to those obtained when solving dynamic equations. In this case, the equations for the probability density are linear, which is indicative of determinism similar to that given by the equations of quantum theory.

Linear properties of the equations of quantum theory cause other properties that are convenient for solving equations. In particular, at the beginning of the development of quantum theory, it was possible to formulate a perturbation theory that allows to effectively solve problems that cannot be solved analytically and to obtain qualitative consequences. If a small parameter can be selected in the problem, then the solution of the equations (wave function, probability density, average values of physical quantities) can be obtained as a power expansion of this parameter. However, if the equations for the probability density of classical nonlinear systems in a state of chaos turn out to be linear, then in the presence of a small parameter, perturbation theory should also work, so that small perturbations should lead to small corrections. The average values of physical quantities should be represented as a small parameter expansion. The paper provides an example of the simplest of such systems and tests its properties by a numerical experiment.

The Duffing equation. Regular and chaotic solutions

The Duffing equations describe forced oscillations in a system with a *W*-potential. Note that the system is highly visual, so it may find use in the educational process (Kondrat'ev, Lyaptsev 2008). In reality, it corresponds to a load that is located in the upper part of the elastic rod and swings in the same plane due to an external force (see Fig. 1). In the absence of external influence, the system has two stable equilibrium positions (*b* and *d*) and one unstable equilibrium position (*c*).

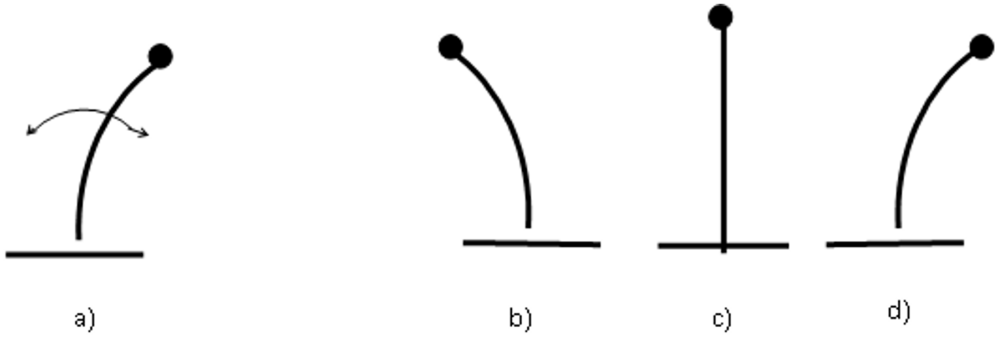

Fig. 1. Model corresponding to the Duffing equation

The oscillation equations have the form:

$$\ddot{x}(t) + \gamma \dot{x}(t) - \alpha x(t) + \beta x^3(t) = F \sin(\omega t)\,. \tag{1}$$

In this equation, the constants α and β characterize the nonlinear elastic force, the constants F and ω—the amplitude and frequency of the external force, and the constant γ—the energy dissipation due to the non-conservative viscous friction force.

Equation (1) can be reduced to a system of three autonomous differential equations of the 1st order:

$$\begin{aligned} \dot{x} &= \upsilon, \\ \dot{\upsilon} &= F\sin\varphi + \alpha x - \beta x^3 - \gamma\upsilon, \\ \dot{\varphi} &= \omega. \end{aligned} \tag{2}$$

Since the system under consideration is dissipative, for any initial conditions, the region of phase space in which the state of the system is located narrows, over time, to the attractor. In the case of regular periodic solutions, the attractor is a closed loop in the phase space. However, for some parameter values, the solution tends to a chaotic (strange) attractor. The dimension of the strange attractor is fractional, and a set of points that is a fractal appears in the section of the phase space with a certain plane. A characteristic property of this system of equations is that with a smooth (adiabatic) change in the control parameter *F*, the state of the system jumps from chaotic motion to regular periodic motion.

The system of equations (2) has a certain symmetry. This means that the system of equations remains invariant with respect to some transformation of variables. In addition to the obvious symmetry $\phi \to \phi + 2\pi$, there is a symmetry with respect to the set of transformations:

$$x \to -x, \quad \upsilon \to -\upsilon, \quad \varphi \to \varphi + \pi\,. \tag{3}$$

Together with the identity transformation, this set of transformations forms a symmetry group isomorphic to the point group $\boldsymbol{C}_s$. Note that a similar system can be considered in the equations of quantum mechanics. In this case, the non-stationary Schrodinger equation determines the eigenvalues of quasi-energies, and the corresponding quasi-energy states are transformed by irreducible representations of the above group, that is, they are even or odd. In this classical case, equations (2) do not imply any properties related to symmetry due to the nonlinearity of the equations. However, numerical calculations (Liaptsev 2013; 2014a; 2014b; 2015) show that the Poincare sections of the phase space with parameters corresponding to the chaotic state are fully symmetric with respect to the transformations (3).

Probabilistic approach

Let us now define a density probability distribution $\rho(\phi, \upsilon, x)$ as follows: for a given value ϕ the value $\Delta w = \rho(\varphi, x, \upsilon)\Delta x\Delta\upsilon$ is equal to the probability that the trajectory of the system passes in the region $[x, x + \Delta x; \upsilon, \upsilon + \Delta\upsilon]$ and the normalization condition is set:

$$\int dx \int d\upsilon \rho\left(\varphi, x, \upsilon\right) = 1, \quad \forall\varphi.$$

Note that the density of the probability distribution can be approximately obtained by a numerical experiment. For this purpose, the section plane needs to be broken into cells , then we perform calculations $x(t)$ and $\upsilon(t)$ over large enough time and put ρ for each cell which is proportional to the number of points that fell into the cell.

The equation for the probability density can be obtained from the Hamilton equations for a classical mechanical system. The derivation of such an equation for a rotator in an external harmonic field is described in detail in (Liapzev 2019). Omitting the derivation of the equation for the system considered here, we give the final expression:

$$\omega\frac{\partial\rho}{\partial\varphi} + \upsilon\frac{\partial\rho}{\partial x} + \left(F\sin\varphi + \alpha x - \beta x^3 - \gamma\upsilon\right)\frac{\partial\rho}{\partial\upsilon} = 0. \tag{4}$$

Equation (4) is a linear first-order partial differential equation. From the theory of differential equations (see (Kamke 1967)) it follows that there are systems of ordinary differential equations associated with a similar differential equation, which, in general, can be written as:

$$\sum_{\nu=1}^{n} f_\nu(x_1, x_2, \ldots, x_n)\frac{\partial\psi(x_1, x_2, \ldots, x_n)}{\partial x_\nu} = 0\,. \tag{5}$$

 DOI: 10.33910/2687-153X-2020-1-4-150-157

The ordinary differential equations have the form:

$$\dot{x}_\nu(t) = f_\nu(x_1, x_2, ..., x_n), \quad \nu = 1, 2, ..., n. \tag{6}$$

Characteristic curves defined by the system of equations (6) are associated with solutions of equation (5). In particular, if $\phi_\nu(t)$ is the solution of a system of equations (6), then if, and only if, the function $\psi(x_1, x_2, ..., x_n)$ is the integral of equation (5) when $\psi(\varphi_1(t), \varphi_2(t), ..., \varphi_n(t)) = \text{const}$ for any characteristic curve. It is easy to verify that in the case under consideration the system of equations that determines the characteristic curves of the equation (4) exactly coincides with the system of equations (2) that determines the dynamics of the system of interest.

One of the methods for solving equations of the form (5) is associated with finding characteristic curves. In our case it can be implemented as finding functions $\rho(\phi, \upsilon, x)$ in the above numerical experiment. However, this is not the only solution. The linear properties of equation (4) allow us to use the Fourier transform for its solution. Since all variables included in the equation are restricted to certain values, the Fourier transform reduces to a multidimensional (in this case, three-dimensional) Fourier series. The numerical solution of the equation can be obtained by restricting the series with some finite values, resulting in a system of linear equations. The accuracy of solutions increases with increasing values that limit the series. In paper (Liapzev 2019), it is shown that the solution obtained by the Fourier transform method for the rotator equation gives a picture of the Poincare sections of the corresponding chaotic attractor similar to the picture obtained by solving dynamic equations.

Perturbation theory for the probability density equation

As mentioned above, the linearity of the equations allows us to obtain their solutions and expressions for the average values of some operators in the form of power expansions of a small parameter. Let us denote the differential operator included in equation (4) by L:

$$L = \omega\frac{\partial}{\partial\varphi} + \upsilon\frac{\partial}{\partial x} + \left(F\sin\varphi + \alpha x - \beta x^3 - \gamma\upsilon\right)\frac{\partial}{\partial\rho},$$

then the equation takes a simple form:

$$L\rho\left(\varphi, x, \upsilon\right) = 0.$$

We now add a small perturbation of the form λV, where V is a certain operator that depends on the variables ϕ, x, υ and the corresponding partial derivatives, and λ is a small parameter introduced to obtain expansions in its powers. Find the function $\rho(\phi, \upsilon, x)$ as a power expansion of this parameter:

$$\rho\left(\varphi, x, \upsilon\right) = \sum_{n=0}^{N} \lambda^n \rho^{(n)}\left(\varphi, x, \upsilon\right). \tag{7}$$

The maximum value of degree of parameter λ in expansion (7) is determined not so much by the accuracy with which the calculation is performed, but, rather, by the qualitative effects obtained at certain degrees of the parameter. For example, in the theory of molecular spectra, the effective small parameter included in the quantum molecular Hamiltonian is the Born—Oppenheimer parameter: $\kappa = \sqrt[4]{m/M}$, where m is the mass of the electron and M is the average mass of the molecule nuclei. In the zero approximation for this parameter, the electronic, vibrational, translational, and rotational motions of the molecule are separated, and the effects due to the interaction of these motions are manifested in certain degrees of expansion of eigenvalues and eigenfunctions on this parameter (Kiselev, Lyapcev 1989).

Finding the terms of the expansion (7) is reduced to a sequential separation from the equation:

$$\left(L + \lambda V\right)\sum_{n=0}^{N} \rho^{(n)}\left(\varphi, x, \upsilon\right) = 0, \tag{8}$$

equations for a given degree of the parameter λ. In zero order, we get the equation:

$$L\rho^{(0)}\left(\varphi, x, \upsilon\right) = 0,$$

corresponding to equation (4). The equation of the 1st order:

$$L\rho^{(1)}(\varphi,x,v)+V\rho^{(0)}(\varphi,x,v)=0$$

allows us to find the first term of the probability density expansion:

$$\rho^{(1)}=-L^{-1}V\rho^{(0)},$$

where L^{-1} on the right side of the equality is the inverse operator of L. Similarly, the following terms of the expansion of the function $\rho(\phi, v, x)$ can be found.

The solution of the problem by the perturbation method is thus reduced to finding some inverse operators that appear in equations of a given order. In quantum theory, such operators are found as a result of expansion of functions on the eigenfunctions of an unperturbed operator. Here, other methods can be used, for example the Fourier transform mentioned above. It is important that the average value of any operator can also be obtained as a power expansion of a small parameter:

$$\begin{aligned} <A>&=\sum_{n=0}^{N}\lambda^n A^{(n)},\\ A^{(n)}&=\int A(\varphi,x,v)\rho^{(n)}(\varphi,x,v)\,d\varphi dx dv. \end{aligned} \tag{9}$$

Despite the fact that formally the decomposition of the average values of operators begins with zero order over a small parameter, the symmetry properties of the systems under consideration can lead to zero values of the first few terms of the decompositions of some operators. In particular, the zero term of the expansion turns out to be zero if the corresponding operator is not transformed by the full-symmetric representation of the symmetry group of the system under consideration.

Turning to the problem we are considering, it is easy to notice that one of the operators that is transformed by the odd representation of the $\boldsymbol{C}_s$ group is the operator of coordinate x (see transformations (3)). It follows that the average value of the x coordinate for the chaotic state of the system described by the Duffing equation turns out to be zero. A numerical experiment confirms this conclusion. Calculating the average value for a finite time interval gives an average of zero, although due to the statistical properties of the state under consideration, each value differs slightly from zero, that is, there are fluctuations in the zero-average value. A non-zero mean value of the coordinate should be obtained if a perturbation is added to the unperturbed operator L, which disturbs the symmetry of the system. One can offer several similar operators. One of these operators is the operator corresponding to adding an odd degree to the W-potential. This corresponds to adding an even degree to the corresponding potential force. Accordingly, the perturbation operator included in equation (4) will have the form:

$$V_1 = x^2\frac{\partial}{\partial v}\ . \tag{10}$$

It is easy to verify that the operator changes its sign during transformations (3). Another possible way to break the symmetry is to add a component with doubled frequency to the external driving force:

Accordingly, the perturbation operator included in equation (4) will have the form:

$$V_2 = \sin(2\varphi)\frac{\partial}{\partial v}\cdot \tag{11}$$

Note that a linear combination of these operators can be used as a perturbation. Then the first order corrections to the average value of the x coordinate will be expressed as a linear function of the corresponding small parameters. In the second order of the perturbation theory, corrections that are a quadratic function of small parameters will appear, and so on.

We denote small parameters for operators V_1 and V_2 by λ_1 and λ_2. Then the system of equations (2) takes the form:

$$\begin{aligned} \dot{x}&=v\\ \dot{v}&=F\sin\varphi+\alpha x-\beta x^3-\gamma v+\lambda_1 x^2+\lambda_2\sin(2\varphi),\\ \dot{\varphi}&=\omega \end{aligned} \tag{12}$$

and the equation for the probability density is:

 DOI: 10.33910/2687-153X-2020-1-4-150-157

$$\omega\frac{\partial\rho}{\partial\varphi}+\upsilon\frac{\partial\rho}{\partial x}+\left(F\sin\varphi+\alpha x-\beta x^3-\gamma\upsilon+\lambda_1 x^2+\lambda_2\sin\left(2\varphi\right)\right)\frac{\partial\rho}{\partial\upsilon}=0\ . \tag{13}$$

The average values of the x coordinate can be calculated either by applying perturbation theory to equation (13) and then using averaging by formula (9), or by solving the system of equations (12) and then averaging the function $x(t)$ over time. Note that it does not follow from the system (12) itself that in the case of a chaotic solution of the system, averaging the coordinate over time for different values of λ_1 and λ_2 will give a linear function of these parameters. Thus, a numerical experiment consisting in obtaining the average coordinate value by solving the system (12) is actually equivalent to a real experiment in relation to proving the applicability of the equation for probability density to the system described by the Duffing equation.

Results of a numerical experiment

We present the results of a numerical experiment for the next values of the parameters included in the system of equations (12): $\alpha = \beta = 1$, $\omega = 1.2$, $\gamma = 0.1$. The value of the parameter F was chosen in such a way that the solution of the system of equations remained chaotic in a certain range of parameters λ_1 and λ_2. Collapse to a regular (periodic) solution for certain values of parameters led to the fact that the corresponding solution was unsuitable for conducting a numerical experiment, since the equation for the probability density is not applicable if the attractor of the equations is a closed line. Below we present the results of a numerical experiment for the values: $F = 5.4$ and $F = 8.7$. In both cases, the averaging was performed over a time interval equal to 10.000 periods of external force, respectively: $\Delta t = 5.236 \cdot 10^4$.

The results of the numerical experiment can be represented as:

$$< x >= y_1\lambda_1 + y_2\lambda_2\ ,$$

where the coefficients y_1 and y_2 were determined from the calculated values for a certain set of parameters λ_1 and λ_2 by the method of least squares. The least squares method also makes it possible to identify the error in determining these coefficients.

Results for F = 5.4.

Parameter λ_1 changed from –0.4 to 0.4 in increments of 0.1, parameter λ_2 changed from –0.15 to 0.15 in increments of 0.05. The results are shown in Table 1.

The deviations of the calculated values from the plane defined by the parameters y_1 and y_2 can be clearly seen in Fig. 2, where the calculated values are shown in circles.

Table 1. Calculation results for F = 5.4

	Values of coefficients	Absolute error	Relative error
Calculation for $\lambda_2 = 0$ and variation of λ_1	$y_1 = 0.344$	$\Delta y_1 = 0.005$	$\delta y_1 = 0.01$
Calculation for $\lambda_1 = 0$ and variation of λ_2	$y_2 = -0.36$	$\Delta y_2 = 0.02$	$\delta y_2 = 0.04$
Calculation for variation of λ_1 and λ_2	$y_1 = 0.301$ $y_2 = -0.37$	$\Delta y_1 = 0.004$ $\Delta y_2 = 0.01$	$\delta y_1 = 0.016$ $\delta y_2 = 0.03$

Results for F = 8.7.

Parameter λ_1 changed from –0.4 to 0.4 in increments of 0.1, parameter λ_2 changed from –0.6 to 0.6 in increments of 0.2. The results are shown in Table 2.

Table 2. Calculation results for F = 8.7

	Values of coefficients	Absolute error	Relative error
Calculation for $\lambda_2 = 0$ and variation of λ_1	$y_1 = 0.70$	$\Delta y_1 = 0.02$	$\delta y_1 = 0.03$
Calculation for $\lambda_1 = 0$ and variation of λ_2	$y_2 = -0.25$	$\Delta y_2 = 0.01$	$\delta y_2 = 0.04$
Calculation for variation of λ_1 and λ_2	$y_1 = 0.76$ $y_2 = -0.26$	$\Delta y_1 = 0.01$ $\Delta y_2 = 0.01$	$\delta y_1 = 0.02$ $\delta y_2 = 0.03$

The deviations of the calculated values from the plane defined by the parameters y_1 and y_2 can be clearly seen in Fig. 3, where the calculated values are shown in circles.

As can be seen from the above results in a good approximation, with an accuracy of several percent, a linear dependence of the average values of the x coordinate on the parameters λ_1 and λ_2 is observed.

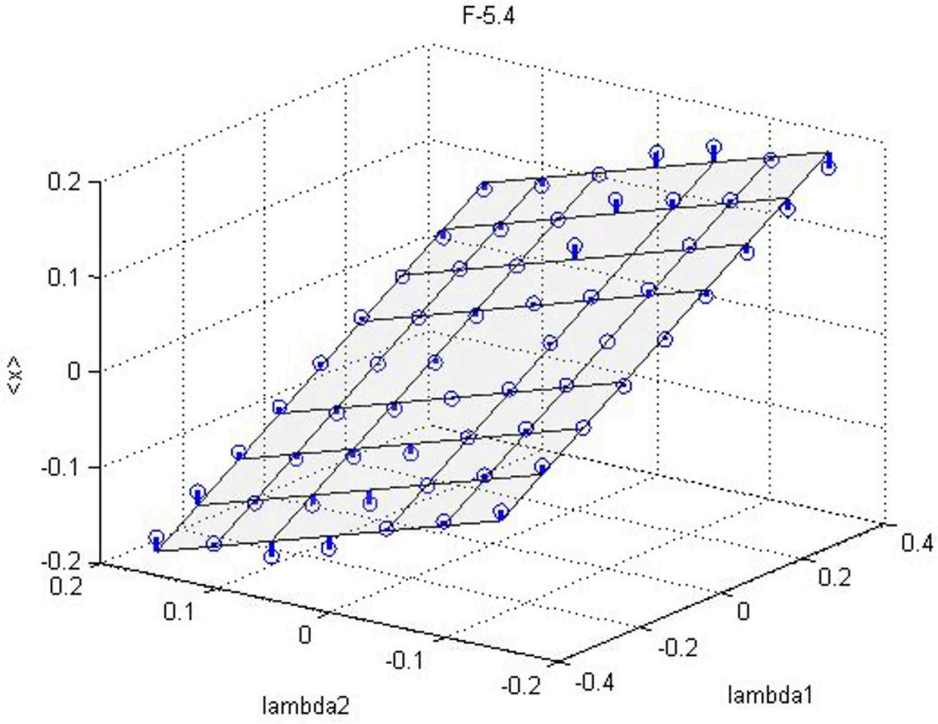

Fig. 2. The deviation of numerical results from the linear dependence at F = 5.4

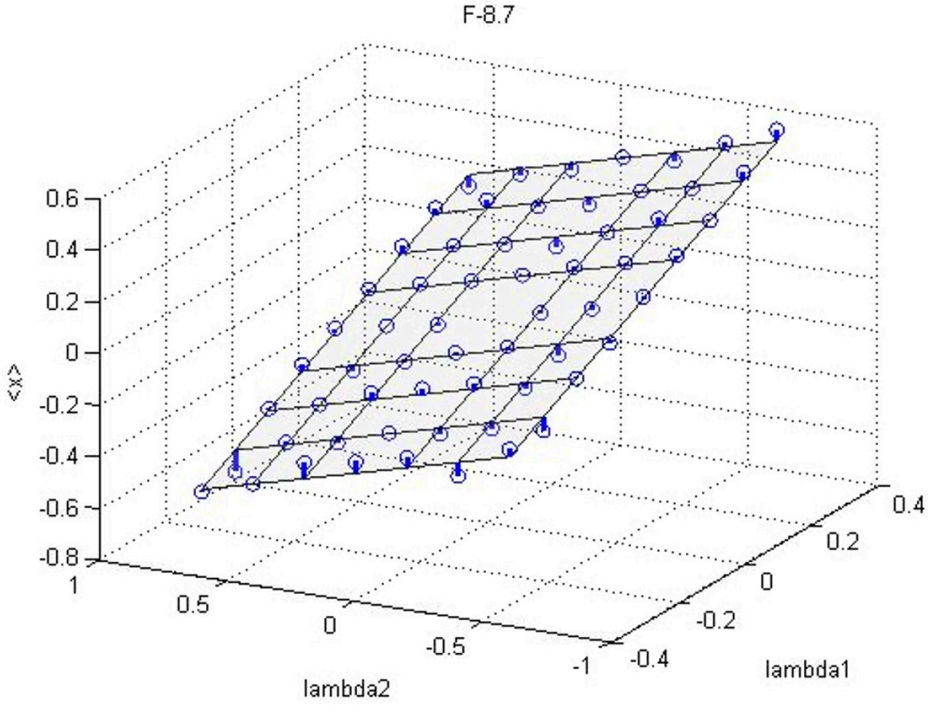

Fig. 3. The deviation of numerical results from the linear dependence at F = 8.7

DOI: 10.33910/2687-153X-2020-1-4-150-157

Conclusion

The results of the numerical experiment show that small perturbations in the system described by the Duffing equation lead to a linear dependence of the average values of physical quantities on small parameters that characterize the perturbation in the chaotic behavior of solutions. This indicates the applicability of perturbation theory to such systems for chaotic solutions. This fact, in turn, can be explained by the fact that the chaotic state of the system can be characterized by a probability density that satisfies the linear equation. Due to the linearity of this equation for small perturbations, the probability density, and, consequently, the average values of physical quantities can be represented as a decomposition in small parameters that characterize the perturbations.

The fact that the chaotic state of a system described by nonlinear dynamic equations can be characterized by a probability density indicates that, despite the non-determinism of classical solutions, in the sense of probability, the chaotic regime is determined to the same extent as the state of the system described in the language of quantum theory.

References

Gonchenko, A. S., Gonchenko, S. V., Kazakov, A. O., Kozlov, A. D. (2017) Matematicheskaya teoriya dinamicheskogo khaosa i ee prilozheniya: Obzor. Chast' 1. Psevdogiperbolicheskie attraktory [Mathematical theory of dynamical chaos and its applications: Review. Part 1. Pseudohyperbolic attractors. Pseudohyperbolic attractors]. *Izvestiya Vysshikh uchebnykh zavedeniy. Prikladnaya nelineynaya dinamika — Izvestiya VUZ. Applied Nonlinear Dynamics*, 25 (2), 4–36. (In Russian)

Kamke, E. (1971) *Differentialgleichungen: Lösungsmethoden und Lösungen. Vol. 2*. Leipzig: Akademische Verlagsgesellschaft, 243 p. (In German)

Kiselev, A. A., Lyapcev, A. V. (1989) *Kvantovomekhanicheskaya teoriya vozmushchenij. Diagrammnyj metod [Quantum mechanical perturbation theory. Diagram method]*. Leningrad: Leningrad State University Publ., 360 p. (In Russian)

Kondrat'ev, A. S., Lyaptsev, A. V. (2008) *Fizika. Zadachi na komp'yutere [Physics. Tasks on the computer].* Moscow: Fizmatlit Publ., 400 p. (In Russian)

Liaptsev, A. V. (2013) Simmetriya regulyarnykh i khaoticheskikh dvizhenij v zadachakh nelinejnoj dinamiki. Uravnenie Duffinga [The symmetry of regular and chaotic motions in nonlinear dynamics problems. Duffing Equation]. *Izvestia Rossijskogo gosudarstvennogo pedagogicheskogo universiteta im. A. I. Gertsena — Izvestia: Herzen University Journal of Humanities & Sciences*, 157, 24–34. (In Russian)

Liaptsev, A. V. (2014a) Simmetriya regulyarnykh i khaoticheskikh dvizhenij v zadachakh nelinejnoj dinamiki. Rotator v periodicheskom pole [Symmetry of regular and chaotic motions in nonlinear dynamic problems. Rotator in periodic field]. *Izvestia Rossijskogo gosudarstvennogo pedagogicheskogo universiteta im. A. I. Gertsena — Izvestia: Herzen University Journal of Humanities & Sciences*, 165, 23–35. (In Russian)

Liaptsev, A. V. (2014b) Simmetriya v zadachakh nelinejnoj dinamiki. Proyavlenie svojstv simmetrii v polyarizatsii izlucheniya [Symmetry in problems of nonlinear dynamics. The manifestation of the properties of the symmetry in the polarization of radiation]. *Izvestia Rossijskogo gosudarstvennogo pedagogicheskogo universiteta im. A. I. Gertsena — Izvestia: Herzen University Journal of Humanities & Sciences*, 168, 16–28. (In Russian)

Liaptsev, A. V. (2015) Proyavlenie svojstv simmetrii v zadachakh nelinejnoj dinamiki. Effekty, analogichnye vyrozhdeniyu v kvantovomekhanicheskikh zadachakh [Manifestation of symmetry properties in problems of nonlinear dynamics. Effects analogous to degeneration in quantum mecanical problems]. *Izvestia Rossijskogo gosudarstvennogo pedagogicheskogo universiteta im. A. I. Gertsena — Izvestia: Herzen University Journal of Humanities & Sciences*, 173, 64–77. (In Russian)

Liapzev, A. V. (2019) The calculation of the probability density in phase space of a chaotic system on the example of rotator in the harmonic field. *Computer Assisted Mathematics*, 1, 55–65. (In English)

Loskutov, A. Yu. (2007) Dynamical chaos: Systems of classical mechanics. *Physics-Uspekhi*, 50 (9), 939–964. DOI: 10.1070/PU2007v050n09ABEH006341 (In English)

Sagdeev, R. Z., Usikov, D. A, Zaslavskii, G. M. (1988) *Nonlinear physics: From the pendulum to turbulence and chaos*. 2nd ed. Chur: Harwood Academic Publ., 675 p. (In English)

Theoretical Physics. Quantum Mechanics

UDC 517.938 DOI: 10.33910/2687-153X-2020-1-4-158-164

A model of a quantum waveguide multiplexer

A. M. Vorobiev[1], T. S. Yurova[1], I. Yu. Popov✉[1]

[1] ITMO University, 49 Kronverksky Ave., Saint Petersburg 197101, Russia

Authors
Alexei M. Vorobiev
Tatiana S. Yurova
Igor Yu. Popov, ORCID: 0000-0002-5251-5327, e-mail: popov1955@gmail.com

For citation: Vorobiev, A. M., Yurova, T. S., Popov, I. Yu. (2020) A model of a quantum waveguide multiplexer. *Physics of Complex Systems*, 1 (4), 158–164. DOI: 10.33910/2687-153X-2020-1-4-158-164

Received 10 October 2020; reviewed 5 November 2020; accepted 5 November 2020.

Funding: This work was partially financially supported by the Government of the Russian Federation (grant 08-08), by grant 16-11-10330 of Russian Science Foundation.

Abstract. The paper explores the system of quantum waveguides and resonators. It suggests a solvable model of zero-width coupling windows based on the operator extensions theory in the Pontryagin space with indefinite metrics. The model self-adjoint operator is constructed explicitly, and it is similar (in some sense) to that of a physical system. We obtain an expression for the transmission coefficient for electrons and investigate its dependence on the electron energy which has a resonant character. It allows to control the electron transmission to different waveguides. The paper proposes a model of a three-channel quantum mesoscopic multiplexer.

Keywords: quantum waveguide, transmission, resonance, operator extensions theory, mesoscopic system.

Introduction

Development of nanotechnology and miniaturization of electronic devices causes the necessity to take into account quantum properties of electron. It is a challenge, yet, it opens a possibility of designing novel devices based on quantum principles. One of such promising developments is a quantum computer. Currently, there are a few quantum computers in operation, however, they are very complicated and are not effective enough. Existing quantum computers can operate with a small number of quantum bits. The scaling of such devices is a great challenge. A possible solution to this challenge lies in the background improvements, e.g. in the use of triadic logic devices. The paper proposes a quantum multiplexer for the triadic logic device and develops a model to describe its processes. It deals with a system of coupled quantum waveguides (quantum wires) and quantum resonators (quantum dots). To describe the electron transmission through the system, we suggest using a model of zero-width coupling windows which has some advantages. Namely, it is solvable, i. e. it yields analytical results. On the other hand, its properties are similar to those of the corresponding physical system. The model has proven to be effective in many cases, see (Pavlov et al. 2001; Popov, Popova 1993a).

The paper focuses on two-dimensional quantum mesoscopic systems, i. e. the physical systems where the electron phase coherence is preserved at a scale much larger than the atomic dimensions. For such systems, quantum properties play an important role (Landauer 1957; Sols et al. 1989; Takagaki, Ploog 1994). The studies of low-dimensional systems usually rely on the Landauer-Buttiker theory (Beenakker, van Houten 1991; Buttiker 1993; Landauer 1970) with its direct relation between the conductivity and the transmission coefficient for ballistic channels.

We consider waveguides connected with resonators through small apertures. It is very difficult to give a full description of such system (Exner, Kovarik 2015; Nazarov et al. 2019). For this reason, we propose an explicitly solvable model which preserves the main features of the corresponding real system. The model is analogous to the zero-range potential approach in quantum mechanics (Albeverio et al. 2005; Pavlov 1987). It is based on the theory of self-adjoint extensions of symmetric operators. The model of resonators coupled through small openings was suggested in (Melikhova, Popov 2017; Popov 1992; 1997; 2013). Resonance effects in the waveguide-resonator-waveguide system in the framework of the model were the focus of (Popov, Popova 1993a; 1993b).

The paper is structured as follows: the first section provides a brief overview of a general mathematical scheme; section two focuses on the implementation of the model for the system of a branching quantum waveguide with inserted quantum resonators; finally, we discuss a possibility to apply the model to the development of a nanoelectronic device.

General mathematical scheme

The conventional operator extension theory approach to the description of resonators coupled through small windows may be found in (Vorobiev et al. 2019). Let us consider two domains Ω_1, Ω_2 with smooth boundaries having a common point r_0. The initial self-adjoint operator for the model construction is the orthogonal sum of the Laplace operators in the domains. The next steps depend on the boundary conditions. In the case of the Neumann boundary conditions, the restriction of the operator on the set of functions vanishing at point r_0 gives a symmetric non-self-adjoint operator with deficiency indices (2,2). Correspondingly, a self-adjoint extension of the operator may be constructed. It is the operator which gives us the model in question. In the case of the Dirichlet boundary conditions, the restricted operator is essentially self-adjoint, i. e. it has deficiency indices (0,0). To construct the model for this boundary condition, it is necessary to extend the space L_2 by adding elements with greater singularities at the point r_0. As a result, we have to deal with the Pontryagin space.

Let us briefly describe the model for the Dirichlet case (Popov 1992) using an indefinite scalar product. Let $\Delta^{1,2}$ be the Laplace operators with the Dirichlet boundary conditions in the domains $\Omega^{1,2}$ with smooth boundaries having a common point r_0. There are two ways of including functions with higher singularities into the space: either considering weighted space or deal with an indefinite scalar product. We follow the latter. Let us consider the following function:

$$h_{-1}^{1,2} = \frac{\partial}{\partial n_y} G^{1,2}\left(r, r', k_0\right)\Big|_{r'=r_0},$$

which does not belong to L_2. Here, $G^{1,2}$ is the Green function for the Dirichlet problem in $\Omega^{1,2}$. Let us define the following set of functions:

$$A^{1,2} = \left\{ f\left(r\right) : f \in L_2\left(\Omega^{1,2}\right), \int_{\Omega^{1,2}} \left| f\left(r\right)\right| \left| r - r_0\right|^{-2} dr < \infty \right\}.$$

Functions from this set have roots of at least first multiplicity at r_0. It is necessary to ensure the integral convergence. Let us consider a pair of functions:

$$h_{-1}^{1,2}, \quad h_1^{1,2} = \left(-\Delta^{1,2} - \lambda_0\right)^{-1} h_{-1}^{1,2}.$$

Here k_0 is some imaginary number ($k_0^2 = \lambda_0$ is a regular point of the Laplace operator in $\Omega^{1,2}$). Now, we introduce another set of functions having singularities $\tilde{A}^{1,2}$:

$$\tilde{A}^{1,2} = \left\{ \tilde{f}^{1,2} : \tilde{f}^{1,2} = f^{1,2} + C_1^{1,2} h_1^{1,2} + C_{-1}^{1,2} h_{-1}^{1,2} \right\}.$$

Here, the first term in the right-hand side is smooth: $f^{1,2} \in \tilde{A}^{1,2}$. It is necessary to define a scalar product in $\tilde{A}^{1,2}$. It can be made in the following way:

$$(\check{f}, \check{g})_{\tilde{A}^{1,2}} = (f, g)_{L_2} + f_{\Omega^{1,2}} \int_{\Omega^{1,2}} f(r) \overline{(C_1^g h_1^{1,2} + C_{-1}^g h_{-1}^{1,2})} + f_{\Omega^{1,2}} g(r)(C_1^f h_1^{1,2} + C_{-1}^f h_{-1}^{1,2}) dr$$

$$+ C_1^f \overline{C_1^g} (h_1^{1,2}, h_1^{1,2})_{L_2} + (C_1^f C_{-1}^g + C_{-1}^f \overline{C_1^g})(h_{-1}^{1,2}, h_1^{1,2})_{L_2}.$$

The set $\tilde{A}^{1,2}$ is not yet a full space. It is embedded into the Pontryagin space Π_1 by conventional way (Derkach et al. 2003; Popov 1992; Shondin 1988; van Diejen, Tip 1991).

Now, it is necessary to define the Laplace operator in this extended space. Let the domain of the operator $\tilde{\Delta}^1$ have the form:

$$D\left(\tilde{\Delta}^1\right)=\left\{\check{f}:\check{f}\in\tilde{A}^1, f\in W_2^{2,loc}\left(\Omega^1\right), f=f_1+Ch_1^1\right\}.$$

Here, $f_1, \left(-\tilde{\Delta}^1-\lambda_0\right)f_0\in A^1$. On the set A^1 the operator $\tilde{\Delta}^1$ acts as the Laplace operator and on the chain h_p^1 the operator $\left(-\tilde{\Delta}^1-\lambda_0\right)$ is a shift operator: $\left(-\tilde{\Delta}^1-\lambda_0\right)h_1^1=h_{-1}^1$. One can prove that the operator $-\tilde{\Delta}^1$ is self-adjoint.

The next step of the model construction is the so-called "restriction-extension" procedure. Let us restrict the operator $-\tilde{\Delta}^1$ onto the following set:

$$D\left(\Delta_0^1\right)=\left\{f:f\in D\left(\tilde{\Delta}^1\right),\left(\left(-\tilde{\Delta}^1-\lambda_0\right)f,h_{-1}^1\right)=0\right\}.$$

The obtained operator Δ_0^1 is symmetric and has deficiency indices (1,1) in the Pontryagin space. The construction procedure for the second domain for Ω^2 is the same. Correspondingly, the orthogonal sum $\Delta_0=\Delta_0^1\oplus\Delta_0^2$ is a symmetric operator with deficiency indices (2,2). Its self-adjoint extensions are restrictions of the adjoint operator. It is easy to describe the domain of the adjoint operator:

$$D\left(\tilde{\Delta}_0^*\right)=\left\{\check{f}:\check{f}\in\tilde{A}^1, f=f_1+Ch_1^1\right\}.$$

Here, $f_1, \left(-\tilde{\Delta}^1-\lambda_0\right)f_1\in A^1$. To construct a self-adjoint extension one should find a linear set of elements from $D\left(\Delta_0^*\right)$ satisfying the self-adjointness condition:

$$J\left(f,g\right)=\left(\left(-\tilde{\Delta}_0^*-\lambda_0\right)\tilde{f},\check{g}\right)-\left(\tilde{f},\left(-\tilde{\Delta}_0^*-\lambda_0\right)\check{g}\right).$$

One can see that elements of $D\left(\Delta_0\right)$ are such elements from $D\left(\tilde{\Delta}\right)$ that satisfy the condition $C_1^1=C_1^2=0$. Taking into account the known asymptotics of the Green function near the boundary point, we obtain the following:

$$J\left(f,g\right)=C_1^{f,1}\overline{C_{-1}^{g,1}}-C_{-1}^{f,1}\overline{C_1^{g,1}}+C_1^{f,2}\overline{C_{-1}^{g,2}}-C_{-1}^{f,2}\overline{C_1^{g,2}}.$$

Geometrical treatment of Lagrange planes leads to the following statement:

Theorem 1. *The set of self-adjoint extensions of the operator $-\Delta_0$ consists of the sets of operators $\{-\Delta_A\}$, $\{-\Delta_B\}$, the domains of which consist of all elements from $D(\Delta_0^*)$ satisfying the conditions*

$$\begin{pmatrix} C_1^1 \\ C_1^2 \end{pmatrix}=\begin{pmatrix} a_{11} & a_{12} \\ a_{21} & a_{22} \end{pmatrix}\begin{pmatrix} C_{-1}^1 \\ C_{-1}^2 \end{pmatrix}$$

or

$$\begin{pmatrix} C_{-1}^1 \\ -C_{-1}^2 \end{pmatrix}=\begin{pmatrix} b_{11} & b_{12} \\ b_{21} & b_{22} \end{pmatrix}\begin{pmatrix} C_1^1 \\ C_{-1}^2 \end{pmatrix},$$

inhere A, B are Hermitian matrices.

Remark. We have no goal to describe all possible extensions. We deal with one extension only corresponding to the following matrix (Popov 1992).

$$b_{11}=b_{22}=0,\ b_{12}=b_{21}=-1 \tag{1}$$

 DOI: 10.33910/2687-153X-2020-1-4-158-164

The system of coupled waveguides and resonators

Let us consider the problem of electron scattering in the system of coupled quantum waveguides and resonators (Fig. 1). The construction of the model operator is the same as in the case of the two coupled domains described above.

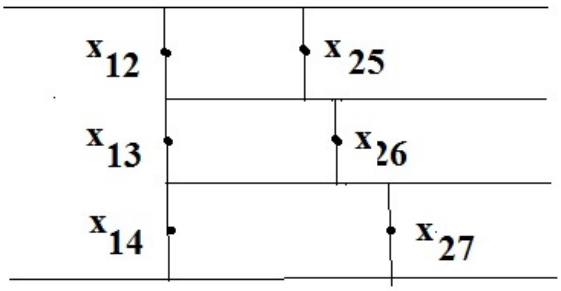

Fig. 1. The geometry of the system. Coupling points are marked

We choose "the most natural" extension (see remark at the end of the previous section). In this case the solution of the scattering problem for the model operator has the form:

$$\psi(r,k)=\begin{cases}\psi_0(r,k)+\alpha_{12}\dfrac{\partial G_1}{\partial x}(r,r_{12},k)+\alpha_{14}\dfrac{\partial G_1}{\partial x}(r,r_{14},k),\\ -\alpha_{12}\dfrac{\partial G_2}{\partial x}(r,r_{12},k)-\alpha_{25}\dfrac{\partial G_2}{\partial x}(r,r_{25},k),\\ -\alpha_{13}\dfrac{\partial G_3}{\partial x}(r,r_{13},k)-\alpha_{36}\dfrac{\partial G_3}{\partial x}(r,r_{36},k),\\ -\alpha_{14}\dfrac{\partial G_4}{\partial x}(r,r_{14},k)-\alpha_{47}\dfrac{\partial G_4}{\partial x}(r,r_{47},k),\\ \alpha_{25}\dfrac{\partial G_5}{\partial x}(r,r_{25},k),\\ \alpha_{36}\dfrac{\partial G_6}{\partial x}(r,r_{36},k),\\ \alpha_{47}\dfrac{\partial G_4}{\partial x}(r,r_{47},k),\end{cases} \tag{2}$$

Here $G_j(r, r_i, k)$ is the Green function for the Dirichlet problem in $\Omega_j, r = (x, y)$, $\psi_0(r, k)$ is the solution of the scattering problem for a semi-infinite waveguide Ω_1 without point-like coupling windows (the sum of incoming and reflected waves), α_{mn} are coefficients to be determined. Taking info account, Theorem 1 and (l) one obtains the following linear system for α_{mn}:

$$\begin{aligned}&\alpha_{12}g_1(r_{12},k)+\alpha_{13}\frac{\partial G_1}{\partial x}(r_{12},r_{13},k)+\alpha_{14}\frac{\partial G_1}{\partial x}(r_{12},r_{14},k)+\frac{\partial\psi_0}{\partial x}(r_{12},k)\\ &\quad=\alpha_{12}g_1(r_{12},k)+\alpha_{25}\frac{\partial G_2}{\partial x}(r_{12},r_{25},k),\\ &\alpha_{25}g_2(r_{25},k)+\alpha_{12}\frac{\partial G_2}{\partial x}(r_{25},r_{12},k)=\alpha_{25}g_5(r_{25},k),\\ &\alpha_{13}g_1(r_{13},k)+\alpha_{12}\frac{\partial G_1}{\partial x}(r_{13},r_{12},k)+\alpha_{14}\frac{\partial G_1}{\partial x}(r_{13},r_{14},k)+\frac{\partial\psi_0}{\partial x}(r_{13},k)\\ &\quad=\alpha_{13}g_3(r_{13},k)+\alpha_{36}\frac{\partial G_3}{\partial x}(r_{36},r_{13},k),\end{aligned} \tag{3}$$

$$\alpha_{36} g_3(r_{36},k) + \alpha_{13} \frac{\partial G_3}{\partial x}(r_{36},r_{13},k) = \alpha_{36} g_6(r_{36},k),$$

$$\alpha_{14} g_1(r_{14},k) + \alpha_{12} \frac{\partial G_1}{\partial x}(r_{14},r_{12},k) + \alpha_{13} \frac{\partial G_1}{\partial x}(r_{14},r_{13},k) + \frac{\partial \psi_0}{\partial x}(r_{14},k)$$

$$= \alpha_{14} g_4(r_{14},k) + \alpha_{47} \frac{\partial G_4}{\partial x}(r_{14},r_{47},k),$$

$$\alpha_{47} g_4(r_{47},k) + \alpha_{14} \frac{\partial G_4}{\partial x}(r_{14},r_{47},k) = \alpha_{47} g_7(r_{47},k),$$

here

$$g_i(r_{jl},k) = \left(\frac{\partial G_i}{\partial x}(r,r_{jl},k) - \frac{\partial G_i}{\partial x}(r,r_{jl},k_0) \right)\Big|_{r \to r_{jl}},$$

k_0 is a model parameter. To choose it, one can compare the solutions of the model and realistic problems. This analysis showed (Popov 1992; 2013) that small width corresponds to large k_0. Moreover, it is possible to choose the parameter in such a way that the model solution gives one the main asymptotic term (in the width of the window) of the corresponding realistic problem. We assume that all coupling windows are identical, in opposite case, it is necessary to introduce several parameters k_{0j} (one for each window). The expression for $\frac{\partial G_i}{\partial x}(r,r',k)$ for a semi-infinite waveguide is well known:

$$\frac{\partial G_i}{\partial x}(r,r',k) = \frac{\partial}{\partial x'} \sum_{n-1}^{\infty} \frac{2 \sin \frac{\pi n y}{d_j} \sin \frac{\pi n y'}{d_j}}{d_j \sqrt{\frac{\pi^2 n^2}{d_j^2} - k^2}} \left(\exp\left(i \sqrt{\frac{\pi^2 n^2}{d_j^2} - k^2} \, |x - x'| \right) \right.$$

$$\left. - \exp\left(i \sqrt{\frac{\pi^2 n^2}{d_j^2} - k^2} \, |x - x^*| \right) \right),$$

where x^* is a mirror image of the point x with respect to the end of the waveguide. Expression for $g_2(r_{12},k)$ (and, correspondingly, for $g_4(r_{14},k)$, $g_3(r_{13},k)$) is

$$g_2(r_{12},k) = \left(k^2 - k_0^2\right) \sum_{n,m=1}^{\infty} \frac{4\pi^2 n^2 \sin^2 \frac{\pi m}{2}}{d_5 l_2^3 \left(\frac{\pi^2 n^2}{l_2^2} + \frac{\pi^2 m^2}{d_5^2} - k^2 \right) \left(\frac{\pi^2 n^2}{l_2^2} + \frac{\pi^2 m^2}{d_5^2} - k_0^2 \right)}.$$

One can solve system (3) and obtain coefficients α_{25}, α_{36}, α_{47}, which give us the transmission coefficients for channels Ω_5, Ω_6, Ω_7, correspondingly.

Discussion

Let us consider the particular case for which the calculations were made. Let $d_5 = d_6 = d_7 = d_1/3$, and l_2, l_3, l_4 differs slightly. Let us compute transmission coefficients, i. e. the squares of modulus of coefficients α_{25}, α_{36}, α_{47}, as functions of the electron energy (k^2) for this particular case to show the possibility of using the suggested construction. The dependences have a resonant character. There are resonant peaks when k^2 is close to an eigenvalue of the corresponding resonator (see Fig. 2). The calculations were made for the first two resonant peaks for $d_5 = d_6 = d_7 = 3$, $l_2 = 1$, $l_3 = 1.1$, $l_4 = 1.2$ (in dimensionless units). This effect can be used for construction of a mesoscopic quantum device.

 DOI: 10.33910/2687-153X-2020-1-4-158-164

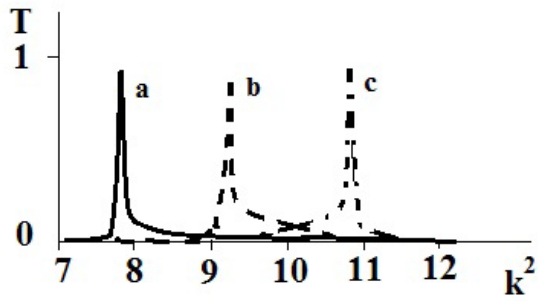

Fig. 2. Transmission coefficients to waveguides 7 (a), 6 (b), 5 (c) via the electron energy k^2 (dimensionless units)

Namely, if electron energy is close an eigenvalue of the resonator Ω_2 we have a resonant transmission to the channel Ω_5 and almost zero transmissions to other channels. Varying electron energy we can obtain resonant transmission to the channel Ω_6 (or Ω_7) with zero fransmissions to other channels. We choose resonators with sizes which change slightly. Hence, small variation of k^2 leads to switching of a signal from one channel to another. Here the control parameter is electron energy.

Another control parameter can be used as well. For example, one can control resonant condition by changing parameters of resonators, or widths of coupling apertures. This can be made by varying the corresponding bias voltage.

In the suggested construction we use resonant properties of coupled resonators, but it is possible to use resonant properties of coupling apertures itself. The existence of such properties was shown for a system of waveguides coupled through small windows in (Popov, Popova 1993a; 1993b) (for the model) and in (Vorobiev et al. 2019) (for a realistic problem). A possible construction based on this effect will be developed and described in the nearest future.

References

Albeverio, S., Gesztesy, F., Hoegh-Krohn, R., Holden, H. (2005) *Solvable models in quantum mechanics*. 2nd ed. S. p.: AMS Chelsea Publishing, 850 p. (In English)

Beenakker, C. W. J., van Houten, H. (1991) Quantum transport in semiconductor nanostructures. *Solid State Physics*, 44, 1–228. DOI: 10.1016/S0081-1947(08)60091-0 (In English)

Buttiker, M. (1993) Capacitance, admittance, and rectification properties of small conductors. *Journal of Physics: Condensed Matter*, 5 (50), article 9361. DOI: 10.1088/0953-8984/5/50/017 (In English)

Derkach, V., Hassi, S., de Snoo, H. (2003) Singular perturbations of self-adjoint operators. *Mathematical Physics, Analysis and Geometry*, 6 (4), 349–384. DOI: 10.1023/B:MPAG.0000007189.09453.fc (In English)

Exner, P., Kovarik, H. (2015) *Quantum waveguides*. Berlin: Springer *Publ.*, 422 p. DOI: 10.1007/978-3-319-18576-7 (In English)

Landauer, R. (1957) Spatial variation of currents and fields due to localized scatterers in metallic conduction. *IBM Journal of research and development*, 1 (3), 223–231. DOI: 10.1147/rd.13.0223 (In English)

Landauer, R. (1970) Electrical resistance of disordered one-dimensional lattices. *The Philosophical Magazine: A Journal of Theoretical Experimental and Applied Physics. Series 8*, 21 (172), 863–867. DOI: 10.1080/14786437008238472 (In English)

Melikhova, A. S., Popov, I. Yu. (2017) Spectral problem for solvable model of bent nano peapod. *Applicable Analysis*, 96 (2), 215–224. DOI: 10.1080/00036811.2015.1120289 (In English)

Nazarov, S. A., Orive-Illera, R., Pérez-Martínez, M.-E. (2019) Asymptotic structure of the spectrum in a Dirichlet-strip with double periodic perforations. *Networks & Heterogeneous Media*, 14 (4), 733–757. DOI: 10.3934/nhm.2019029 (In English)

Pavlov, B. S. (1987) The theory of extensions and explicitly-soluble models. *Russian Mathematical Surveys*, 42 (6), 127–168. DOI: 10.1070/RM1987v042n06ABEH001491 (In English)

Pavlov, B. S., Popov, I. Yu., Frolov, S. V. (2001) Quantum switch based on coupled waveguides. *The European Physical Journal B — Condensed Matter and Complex Systems*, 21 (2), 283–287. DOI: 10.1007/s100510170203 (In English)

Popov, I. Yu. (1992) The resonator with narrow slit and the model based on the operator extensions theory. *Journal of Mathematical Physics*, 33 (11), 3794–3801. DOI: 10.1063/1.529877 (In English)

Popov, I. Yu. (1997) On the point and continuous spectra for coupled quantum waveguides and resonators. *Reports on Mathematical Physics*, 40 (3), 521–529. DOI: 10.1016/S0034-4877(97)85901-0 (In English)

Popov, I. Yu. (2013) Model of point-like window for electromagnetic Helmholtz resonator. *Zeitschrift für Analysis und ihre Anwendungen*, 32 (2), 155–162. DOI: 10.4171/ZAA/1478 (In English)

Popov, I. Yu., Popova, S. L. (1993a) The extension theory and resonances for a quantum waveguide. *Physics Letters A*, 173 (6), 484–488. DOI: 10.1016/0375-9601(93)90162-S (In English)

Popov, I. Yu., Popova, S. L. (1993b). Zero-width slit model and resonances in mesoscopic systems. *Europhysics Letters*, 24 **(5)**, 373–373. DOI: 10.1209/0295-5075/24/5/009 (In English)

Shondin, Yu. G. (1988) Quantum-mechanical models in R_n associated with extensions of the energy operator in a Pontryagin space. *Theoretical and Mathematical Physics*, 74 (3), 220–230. DOI: 10.1007/BF01016615 (In English)

Sols, F., Macucci, M., Ravaioli, U., Hess, K. (1989) Theory for a quantum modulated transistor. *Journal of Applied Physics*, 66 (8), 3892–3906. DOI: 10.1063/1.344032 (In English)

Takagaki, Y., Ploog, K. (1994) Ballistic electron transmission in coupled parallel waveguides. *Physical Review B*, 49 (3), 1782–1788. DOI: 10.1103/PhysRevB.49.1782 (In English)

van Diejen, J. F., Tip, A. (1991) Scattering from generalized point interactions using self–adjoint extensions in Pontryagin spaces. *Journal of Mathematical Physics*, 32 (3), 630–641. DOI: 10.1063/1.529404 (In English)

Vorobiev, A. *V., Bagmutov, A.* S., Popov, A. I. (2019) On formal asymptotic expansion of resonance for quantum waveguide with perforated semitransparent barrier. *Nanosystems: Physics, Chemistry, Mathematics*, 10 (4), 415–419. DOI: 10.17586/2220-8054-2019-10-4-415-419 (In English)

Theoretical Physics.
Physics of Low-Dimensional Structures and Nanostructures

UDC 537.6

DOI: 10.33910/2687-153X-2020-1-4-165-168

Fine energy structure of a magnetic skyrmion localized on a nonmagnetic impurity in an external magnetic field

M. N. Potkina[✉1, 2, 3], I. S. Lobanov[1, 2], V. M. Uzdin[1, 2]

[1] Saint Petersburg State University, 7/9 Universitetskaya Emb., Saint Petersburg 199034, Russia
[2] ITMO University, 49 Kronverksky Ave., Saint Petersburg 197101, Russia
[3] University of Iceland, 2 Sæmundargata, Reykjavík 102, Iceland

Authors

Mariia N. Potkina, ORCID: 0000-0002-1380-2454, e-mail: potkina.maria@yandex.ru

Igor S. Lobanov, ORCID: 0000-0001-8789-3267

Valery M. Uzdin, ORCID: 0000-0002-9505-0996

For citation: Potkina, M. N., Lobanov, I. S., Uzdin, V. M. (2020) Fine energy structure of a magnetic skyrmion localized on a nonmagnetic impurity in an external magnetic field. *Physics of Complex Systems*, 1 (4), 165–168. DOI: 10.33910/2687-153X-2020-1-4-165-168

Received 16 October 2020; reviewed 30 October 2020; accepted 1 November 2020.

Funding: This work was supported by the Russian Foundation of Basic Research (grants No. 18-02-00267 and No. 19-32-90048) and the Foundation for the Advancement of Theoretical Physics and Mathematics "BASIS", Grant No. 19-1-1-12-1,2.

Abstract. The Localization of a magnetic skyrmion on a nonmagnetic defect in a two-dimensional triangular lattice is investigated within the framework of the generalized Heisenberg model, which includes exchange, anisotropy, Dzyaloshinskii–Moriya interaction, and interaction with an external magnetic field. It is shown that there is a threshold magnetic field, below which there are two locally stable positions of the defect inside the skyrmion. The energy difference between the states with a different localization of defects results in a fine energy structure of skyrmions, depending on the strength of the magnetic field.

Keywords: saddle point, minimum energy path, skyrmion, logic device, racetrack memory.

Introduction

A magnetic skyrmion (Sk) is a localized non-collinear state that has been observed, in particular, in thin films of 3d metals on the surface of heavy metals (Hagemeister et al. 2015). The small size and high mobility under the action of ultra-low current density make this system attractive for use in spintronic applications. Sks, like particles, can move freely in a magnetic film while maintaining their size and shape. For their practical use, it is important to be able to localize Sks in a certain area and move them along a definite trajectory. This can be achieved by a local change in the strength of the magnetic interactions or values of those magnetic moments in the media where the Sk is located. Elongated domains (Castell-Queralt et al. 2019) or sample boundaries (Zhang et al. 2015) provide "rails" for the movement of the skyrmion, while local point defects can lead to the formation of a center of attraction or repulsion, or to anchoring the Sk in a certain place (Stosic et al. 2017).

Local point defects can affect the current-induced motion of Sks. Calculations have shown that the introduction of local anisotropy in some sites of the two-dimensional lattice does not change the Sk velocity/current ratio (Iwasaki et al. 2013), but nonmagnetic local impurities change the trajectory of Sks and can pin them, so that a small current will not move the skyrmion along the sample at all (Müller, Rosch 2015).

Nonmagnetic defects also change the activation energy for skyrmion annihilation and nucleation from a ferromagnetic state. Consequently, it may turn out that most of the Sks that will be produced by recording devices will be localized (Romming et al. 2013).

A non-magnetic defect modifies the energy surface of the system and reduces the energy of the transition state. The inclusion of an external magnetic field also leads to a change in the shape of the energy surface, which also reduces the stability of the Sk if the field is directed antiparallel to the magnetization in the skyrmion core (Uzdin et al. 2018). In this paper, we include both factors and study the field dependence of the energy surface of a Sk localized at a nonmagnetic defect.

Model and methods

A thin magnetic film was modelled in a Heisenberg type model with a triangular lattice. Energy E of a magnetic state is given by

$$E = -J\sum_{<i,j>}\vec{S}_i \cdot \vec{S}_j - \sum_{<i,j>}\vec{D}_{ij}\cdot\left[\vec{S}_i \times \vec{S}_j\right] - K\sum_i S_{i,z}^2 - \mu\vec{B}\sum_i \vec{S}_i \,. \quad (1)$$

Here J is the exchange parameter, which is assumed to be non-zero only for the nearest-neighbor sites, $\vec{D}_{ij}$ is the Dzyaloshinskii-Moriya (DM) vector laying in a plane orthogonal to the line connecting atomic sites i and j. The vector of anisotropy is perpendicular to the lattice plane along the z-axis. $K > 0$ is the constant of easy axis anisotropy. Magnetic field $\vec{B} = B\vec{z}$ is directed along the magnetization in homogeneous ferromagnetic state. $\vec{S}_i$ are three-dimensional vectors of unit length along the magnetic moment on site i; μ is the magnitude of the magnetic moments.

A single site is assumed to be a nonmagnetic impurity. The summation $< i, j >$ in (1) is taken over all pairs of the nearest neighbor sites in the triangular lattice excluding the impurity. The values of the parameters taken from (Hagemeister et al. 2015) correspond to the experimentally observed skyrmions in the Pd/Fe/Ir(111) system, $\mu B = 0.093\,J, K = 0.07\,J, D = \left|\vec{D}_{ij}\right| = 0.32\,J, J = 7(\text{meV})$.

The system supports the Neel (hedgehog) Sk slightly disturbed by the presence of impurity. We considered a strip of a triangular lattice containing 80 × 61 atoms with periodic boundary conditions, which is large enough to host an isolated skyrmion, namely, the energy perturbation due to self-interaction across the boundary is about 0.0002%. The dipolar interaction or the demagnetizing field is not taken into account, since the Sks under study have a diameter less than 4.6 nm (the lattice constant for Fe / Ir (111) is 0.27 nm). The impurity is a local disturbance, which should not be affected by the demagnetizing field.

The metastable states of Sks were calculated numerically using the conjugate gradient method in Cartesian coordinates (Lobanov, Uzdin 2020). The transformations of a magnetic Sk localized on an impurity were studied by calculating the minimum energy paths MEPs between the Sk state and the other (meta) stable states on the energy surface of the system. The MEPs were calculated using the geodesic nudge elastic band method (Bessarab et al. 2015).

Localization of an Sk on an impurity in the external magnetic field

The appending of a non-magnetic impurity to the ferromagnetic phase creates an energy vertex around this magnetic defect that repels Sks nearby. However, if the distance from the impurity to the Sk center is approximately equal to the Sk radius, then the Sk is pinned to the impurity, see Fig. 1a, c. The energy landscape has a local minimum for a specific location of the impurity, and the Sk must overcome the activation barrier for the dissociation from the impurity. The equilibrium positions of the defect correspond to the plane orientation of the magnetization $S_z = 0$ and form a "ring". This behavior has been observed experimentally using the scanning tunneling microscopy technique (Hanneken et al. 2016).

We found out that for the external magnetic field weaker than a critical value B_c there exists another possibility for pinning, when the impurity is located exactly in the center of the Sk, see Fig. 1b. For such weak fields, the magnetization in the central part of the Sk is almost uniform and opposite to the magnetization in the ferromagnetic phase, however, the local maximum of energy density is formed in the Sk center. According to our numerical simulation $\mu B = 0.067\,J$, for the parameters under consideration. For larger $B > B_c$, the impurity in the center is not a stable position and the Sk domain wall is attracted by a nonmagnetic hole.

 DOI: 10.33910/2687-153X-2020-1-4-165-168

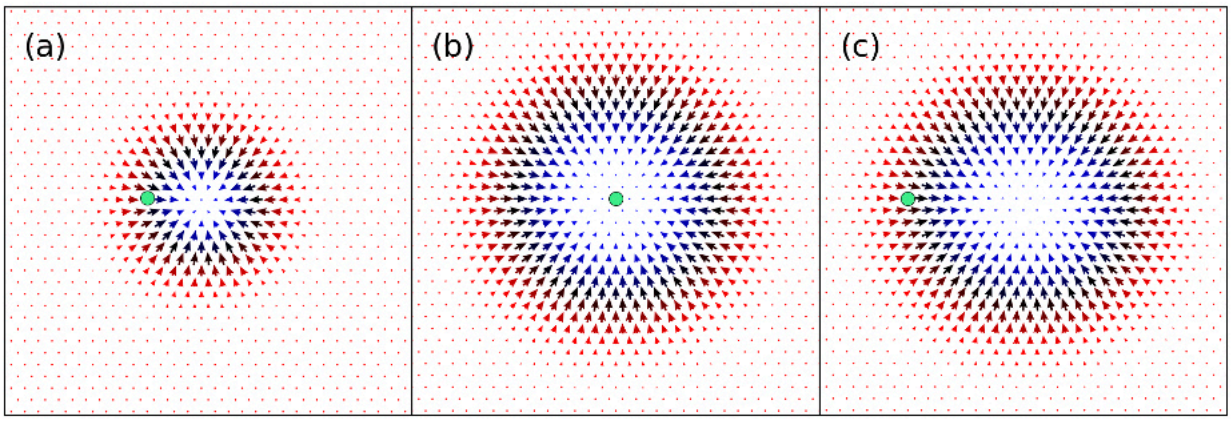

Fig. 1. An isolated Sk with the impurity in the boundary (panels a, c) and in the center (b) for $\mu B = 0.093\,J$ (panel a) and $\mu B = 0.046\,J$ (b, c). The Sk with the impurity in the center is metastable only for B below the critical field $\mu B_c = 0.067\,J$, whereas the impurity at the boundary is metastable down to $\mu B = 0.13\,J$, and the skyrmion without impurities is stable down to $\mu B = 0.21\,J$

The energy barriers for the transition from a state with an impurity in the Sk center to a state with an impurity at the boundary were found by calculating the MEP shown in Fig. 2a. An increase in the external field raises both the energy of the initial and transition states, but the former grows faster than the latter. This is why the energy barrier between the initial and final states tends to zero as $B \to B_c$, which leads to the instability of the central position of the nonmagnetic defect for high fields, see Fig. 2b.

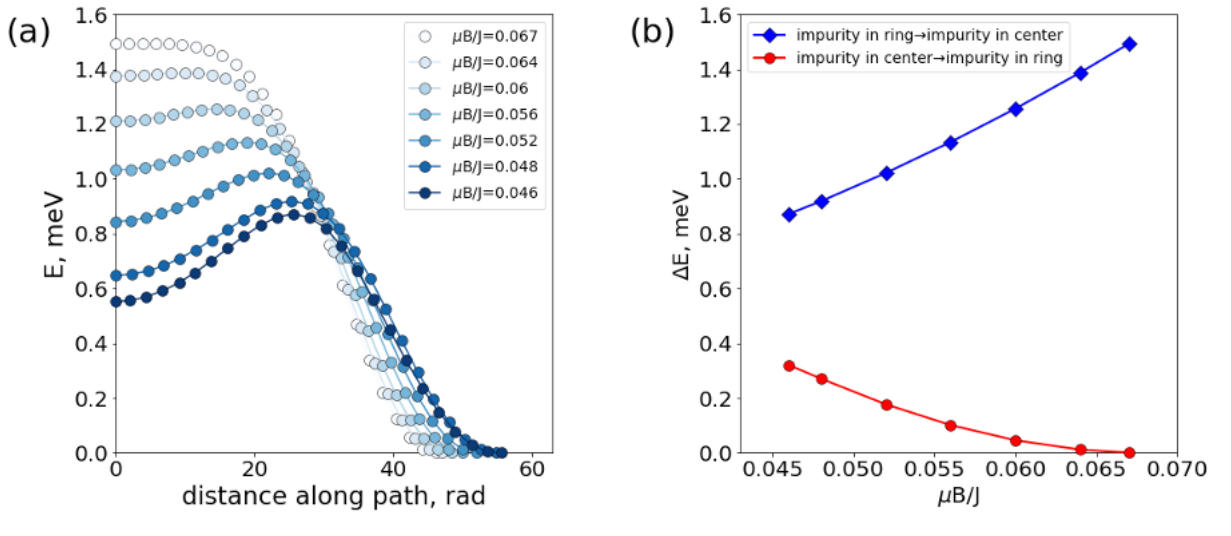

Fig. 2. (a) The minimum energy paths between the states with an impurity in the Sk center and at the Sk boundary for a magnetic field range of $0.046\,J \le \mu B \le 0.067\,J$. The zero energy corresponds to the skyrmion with the impurity at the boundary. (b) The energy barriers for transitions from the state with an impurity in the Sk center to the state with an impurity at the Sk boundary and backward as a function of the magnetic field

To a first approximation, a nonmagnetic impurity can be regarded as the absence of a single spin in an Sk. Then the stable positions of the impurity should correspond to the maximum energy density in the skyrmion. All contributions to the energy of the metastable Sk state are shown in Fig. 3 for two values of the magnetic field below and above the critical one. It can be seen that an Sk is stabilized by the DM interaction, since only this contribution is negative. The impurity at the Sk boundary is, indeed, in the local maximum of the energy density.

When the magnetic field decreases below the critical value B_c, the density of the DM interaction energy increases in the Sk center. Then the second local maximum of total energy density appears near the defect (Fig. 3, lower row) and the removal of the magnetic site from the Sk center gives a maximal local energy reduction.

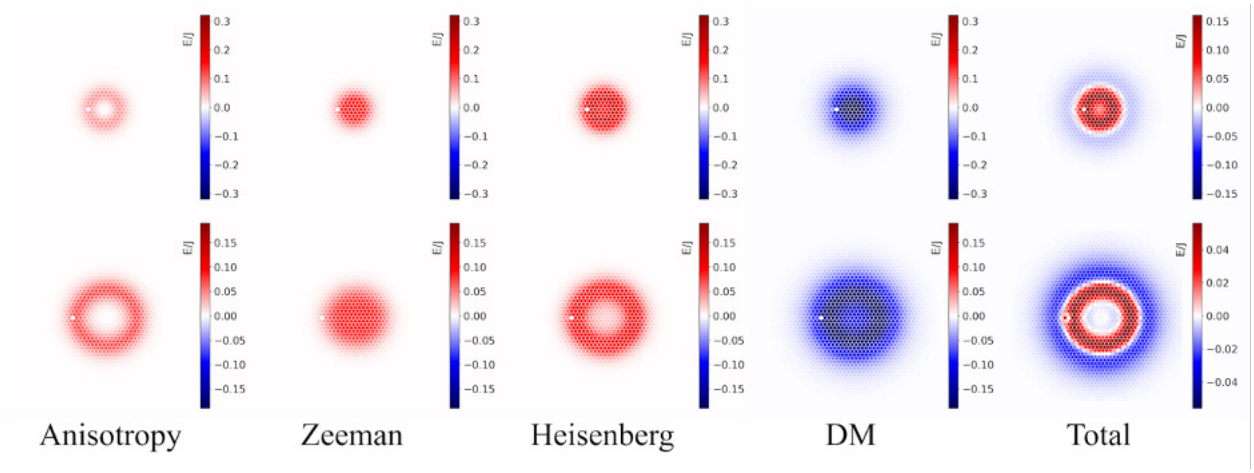

Fig. 3. Contributions of energy per spin in a magnetic field $\mu B = 0.093\ J$ (top row) and $\mu B = 0.046\ J$ (bottom row), the columns correspond to the different contributions of energy. The position of the impurity is shown with a white dot

Conclusions

Calculation of the energy Sk localized at a nonmagnetic defect showed the presence of two local energy minima below the threshold magnetic field B_c. They correspond to the location of the defect at the border and in the very center of the Sk. The energies of these Sk configurations depend on the magnitude of the magnetic field. Therefore, one can expect resonant energy absorption caused by the interaction with current or spin waves in such systems.

References

Bessarab, P. F., Uzdin, V. M., Jónsson, H. (2015) Method for finding mechanism and activation energy of magnetic transitions, applied to skyrmion and antivortex annihilation. *Computer Physics Communications*, 196, 335–347. DOI: 10.1016/j.cpc.2015.07.001 (In English)

Castell-Queralt, J., González-Gómez, L., Del-Valle, N. et al. (2019) Accelerating, guiding, and compressing skyrmions by defect rails. *Nanoscale*, 11 (26), 12589–12594. DOI: 10.1039/C9NR02171J (In English)

Hagemeister, J., Romming, N., von Bergmann, K. et al. (2015) Stability of single skyrmionic bits. *Nature Communications*, 6, article 8455. DOI: 10.1038/ncomms9455 (In English)

Hanneken, C., Kubetzka, A., von Bergmann, K., Wiesendanger, R. (2016) Pinning and movement of individual nanoscale magnetic skyrmions via defects. *New Journal of Physics*, 18 (5), article 055009. DOI: 10.1088/1367-2630/18/5/055009 (In English)

Iwasaki, J, Mochizuki, M., Nagaosa, N. (2013) Universal current-velocity relation of skyrmion motion in chiral magnets. *Nature Communications*, 4, article 1463. DOI: 10.1038/ncomms2442 (In English)

Lobanov, I. S., Uzdin, V. M. (2020) The lifetime of big size topological chiral magnetic states. Estimation of the pre-exponential factor in the Arrhenius law. *arXiv.org. Condensed Matter*, article arXiv:2008.06754. [Online]. Available at: https://arxiv.org/pdf/2008.06754.pdf (accessed 17.09.2020). (In English)

Müller, J., Rosch, A. (2015) Capturing of a magnetic skyrmion with a hole. *Physical Review B*, 91 (5), article 054410. DOI: 10.1103/PhysRevB.91.054410 (In English)

Romming, N., Hanneken, C., Menzel, M. et al. (2013) Writing and deleting single magnetic skyrmions. *Science*, 341 (6146), 636–639. DOI: 10.1126/science.1240573 (In English)

Stosic, D., Ludermir, T. B., Milošević, M. V. (2017) Pinning of magnetic skyrmions in a monolayer Co film on Pt (111): Theoretical characterization and exemplified utilization. *Physical Review B*, 96 (21), article 214403. DOI: 10.1103/PhysRevB.96.214403 (In English)

Uzdin, V. M., Potkina, M. N., Lobanov, I. S., Bessarab, P. F., Jónsson, H. (2018) Energy surface and lifetime of magnetic skyrmions. *Journal of Magnetism and Magnetic Materials*, 459, 236–240. DOI: 10.1016/j.jmmm.2017.10.100 (In English)

Zhang, X., Zhao, G. P., Fangohr, H. et al. (2015) Skyrmion-skyrmion and skyrmion-edge repulsions in skyrmion-based racetrack memory. *Scientific Reports*, 5, article 7643. DOI: 10.1038/srep07643 (In English)